

Post-hoc Probabilistic Vision-Language Models

Anton Baumann^{1*} Rui Li² Marcus Klasson^{2,3} Santeri Mentu^{2,3}
Shyamgopal Karthik^{4,5,6} Zeynep Akata^{1,5,6,7} Arno Solin^{2,3} Martin Trapp²

¹Technical University of Munich ²Aalto University ³Finnish Center for Artificial Intelligence ⁴University of Tübingen
⁵Helmholtz Munich ⁶Munich Center for Machine Learning (MCML) ⁷Munich Data Science Institute (MDSI)

Abstract

Vision-language models (VLMs), such as CLIP and SigLIP, have found remarkable success in classification, retrieval, and generative tasks. For this, VLMs deterministically map images and text descriptions to a joint latent space in which their similarity is assessed using the cosine similarity. However, a deterministic mapping of inputs fails to capture uncertainties over concepts arising from domain shifts when used in downstream tasks. In this work, we propose post-hoc uncertainty estimation in VLMs that does not require additional training. Our method leverages a Bayesian posterior approximation over the last layers in VLMs and analytically quantifies uncertainties over cosine similarities. We demonstrate its effectiveness for uncertainty quantification and support set selection in active learning. Compared to baselines, we obtain improved and well-calibrated predictive uncertainties, interpretable uncertainty estimates, and sample-efficient active learning. Our results show promise for safety-critical applications of large-scale models.

1. Introduction

The rise of foundation models [3, 6, 17, 53] has led to their increasing adoption in downstream tasks where data is scarce [27, 77]. During training, these models are exposed to extensive data sets, sometimes containing billions of data points (e.g., [61, 66]). Pre-trained large-scale vision-language models (VLMs) [75], such as CLIP [53] and SigLIP [74], have shown remarkable performance in various tasks, including classification, retrieval, and generation. To accommodate for concept or domain shifts, few-shot learning (FSL) of VLMs has recently gained increasing attention [34, 41, 64, 73, 76, 78], with methods ranging from fine-tuning to learning linear adapters [64]. However, a critical question in practical applications of FSL is: *Which data to select for adaptation?*

*Work done during an internship at Aalto University.

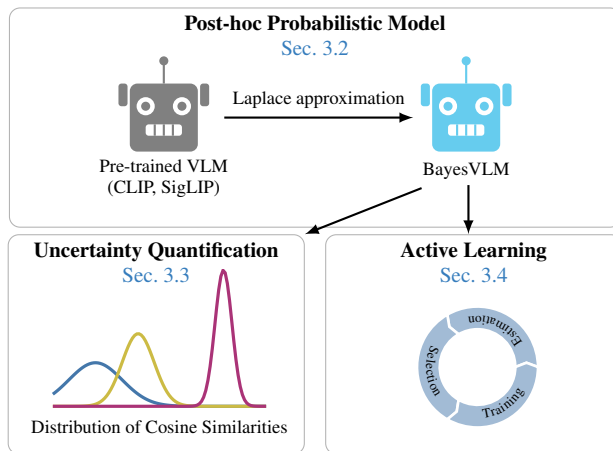


Figure 1. We introduce a principled and efficient post-hoc method to provide uncertainty estimates for vision-language models (e.g., CLIP, SigLIP) using a Laplace approximation. We demonstrate that uncertainty estimates derived from this approximation improve the calibration of these models on several zero-shot classification benchmarks and can be used for active learning.

The paradigm of active learning (or active fine-tuning) [1, 28–30, 47, 71] aims to tackle these challenges by selecting a support set (training set for adaptation) that is most informative for the downstream task. For this, most active learning methods rely on uncertainty [13, 37, 72] and diversity [5] based acquisition function, sometimes called the ‘two faces’ of active learning [14]. Hence, it is crucial to obtain reliable and calibrated uncertainty estimates to select the support set faithfully in real-world settings. However, efficient and accurate uncertainty quantification is a major challenge in large-scale VLMs and typically requires training an additional adapter [10, 68] or changing the training objective [11].

In this work, we propose a principled yet efficient post-hoc uncertainty estimation in VLMs. We first leverage a Laplace approximation [43] to estimate the posterior, eliminating the need for additional training, architectural changes,

or changing the training objective. Then, we derive an analytical expression of the distribution over cosine similarities to efficiently propagate uncertainty in VLMs. Our derived expression applies to any VLM with probabilistic embeddings. To demonstrate the effectiveness of our approach, we evaluate its performance on several classification benchmarks in the zero-shot and active learning setting. In zero-shot learning, we find consistent reductions in the expected calibration error and the negative log predictive density, showing improved calibration. Further, to apply our approach in the active learning setting, we utilise acquisition functions from the Bayesian active learning community [2, 19, 26] in combination with adaptive target region selection through k -nearest neighbour search [44]. We find improvements in performance after targeting the selection using k -nearest neighbour search and further improvements if the estimated uncertainties are incorporated into the selection process, highlighting the viability of our approach for downstream tasks.

Contributions Fig. 1 illustrates the overall contributions of our work, which can be summarised as:

- We propose a principled yet efficient post-hoc method for uncertainty quantification in pre-trained VLMs without needing architecture changes or further training.
- We derive an analytical expression of the distribution over cosine similarities, which allows efficient sampling-free uncertainty propagation in VLMs in zero-shot and few-shot classification settings, applicable to any VLM with probabilistic embeddings.
- We apply our method (BayesVLM) in zero-shot classification and active learning, and qualitatively assessed the interpretability of the distribution over cosine similarities. We show improvements in uncertainty estimation and active learning compared to standard baselines.

2. Related Work

Vision-Language Models Models such as CLIP [53] and SigLIP [74], which are trained on billions of image-text pairs [18, 61], have become widespread in recent years. Their success is partly due to their ability to map images and text to a shared concept space and their success in various tasks, such as zero/few-shot classification, generative modeling [52, 57], and text and multimodal image retrieval [35, 59]. In this work, we demonstrate a principled approach for uncertainty estimation for these pre-trained VLMs.

Probabilistic Vision-Language Models Several works are aiming to extend VLMs to produce predictive uncertainty estimates for various downstream tasks, *e.g.*, cross/multimodal retrieval [10, 38, 48] and visual-question answering [33]. These methods learn probabilistic embeddings on each modality by estimating probability distributions from the network. However, this approach requires training the net-

works from scratch, which limits their applicability to pre-trained VLMs (*e.g.*, CLIP). To this end, there has been recent work [9, 68] that trains an adapter to predict the parameters of the probability distribution. Finally, there have also been attempts to train a probabilistic VLM end-to-end [11] from scratch. Differently, we apply the Laplace approximation to estimate uncertainties directly from the pre-trained VLM in a post-hoc fashion. Our approach only requires access to the pre-training data to estimate the posterior distribution without the need for additional training, architectural changes, or changing the training objective. We demonstrate how these uncertainties can improve the calibration of VLMs in zero/few-shot settings [67] in the experiments.

Active Learning In the active learning setting [55], a machine learning model trained on an initial (possibly small) data source has to determine through an acquisition function which additional data points are needed for making reliable predictions on a given downstream task. For this, the acquisition function quantifies the informativeness of support set candidates for the target task. Various acquisition functions have been studied in the literature, including entropy-based approaches [25], coreset-based approaches [62], and acquisition functions that utilise model uncertainties [2, 19, 26]. A popular approach in the Bayesian active learning community is the Bayesian active learning by disagreement (BALD) score [19, 26], which measures the reduction in epistemic uncertainties of the model. More recently, the expected predictive information gain (EPIG, [2]) was proposed to measure the information gain in the space of predictions rather than parameters. However, those score functions have found little application in large-scale models such as VLMs, where tailored approaches, *e.g.*, through prompt learning [1], are more common. In this work, we focus on transferring knowledge from the Bayesian active learning community to the VLM community.

3. Methods

Notation We denote vectors by bold lower-case letters (*e.g.*, \mathbf{x} , \mathbf{a}) and use bold upper-case letters for matrices (*e.g.*, \mathbf{X} , \mathbf{P}). Further, sets are denoted in upper-case calligraphic letters (*e.g.*, \mathcal{D} , \mathcal{I}) and model parameters or hyperparameters are denoted using Greek letters (*e.g.*, α , θ).

In particular, let $\mathbf{x}_i^{\text{IMG}} \in \mathbb{R}^{p_{\text{IMG}}}$ and $\mathbf{x}_j^{\text{TXT}} \in \mathbb{R}^{p_{\text{TXT}}}$ denote the i^{th} image and j^{th} text description, respectively. Further, let $\phi: \mathbb{R}^{p_{\text{IMG}}} \mapsto \mathbb{R}^{d_{\text{IMG}}}$ and $\psi: \mathbb{R}^{p_{\text{TXT}}} \mapsto \mathbb{R}^{d_{\text{TXT}}}$ denote the image and text encoders of the VLM, where p_{IMG} and p_{TXT} are the respective input dimensionalities and d_{IMG} , d_{TXT} is the dimensionality of the respective feature space. Then we denote the feature embeddings in the joint space as $\mathbf{g} = \mathbf{P}\phi(\mathbf{x}^{\text{IMG}})$ and $\mathbf{h} = \mathbf{Q}\psi(\mathbf{x}^{\text{TXT}})$, where we assume a linear projection denoted by $\mathbf{P} \in \mathbb{R}^{d \times d_{\text{IMG}}}$ and $\mathbf{Q} \in \mathbb{R}^{d \times d_{\text{TXT}}}$. Lastly, we use

the hat symbol to denote unit-length normalised vectors, *e.g.*, $\hat{g} = \frac{g}{\|g\|}$. A detailed notation is listed in App. A.

3.1. Language-Image Pre-training

We consider VLMs trained by minimizing the InfoNCE loss [51] (*e.g.*, CLIP [53]) or the SigLIP loss [74]. Specifically, the InfoNCE loss is defined as the sum of two cross-entropy terms, one for each relational direction—image to text ($\mathcal{L}_{\text{CE}}(\mathbf{X}^{\text{IMG}}, \mathbf{X}^{\text{TXT}})$) and text to image ($\mathcal{L}_{\text{CE}}(\mathbf{X}^{\text{TXT}}, \mathbf{X}^{\text{IMG}})$). The total loss is defined as follows $\mathcal{L}_{\text{InfoNCE}}(\mathbf{X}^{\text{IMG}}, \mathbf{X}^{\text{TXT}}) =$

$$-\frac{1}{2n} \sum_{i=1}^n \log \left(\underbrace{\frac{\exp(t\hat{g}_i^\top \hat{h}_i)}{\sum_{j=1}^n \exp(t\hat{g}_i^\top \hat{h}_j)}}_{\text{IMG} \rightarrow \text{TXT}} \underbrace{\frac{\exp(t\hat{h}_i^\top \hat{g}_i)}{\sum_{j=1}^n \exp(t\hat{h}_i^\top \hat{g}_j)}}_{\text{IMG} \leftarrow \text{TXT}} \right), \quad (1)$$

where t is a learnable temperature parameter, n denotes the number of image-text pairs, and \hat{g} and \hat{h} are the unit-length normalised embeddings. This contrastive loss function has found broad application in training VLMs, as it encourages embeddings for matching image-text pairs to be similar while simultaneously pushing unrelated image-text pairs away [51].

Recently, the SigLIP loss [74] has been proposed as an alternative to the InfoNCE loss, aimed at improving numerical stability and training speed. In contrast to InfoNCE, the SigLIP loss uses a binary classification loss over the cosine similarities, *i.e.*, $\mathcal{L}_{\text{SigLIP}}(\mathbf{X}^{\text{IMG}}, \mathbf{X}^{\text{TXT}}) =$

$$-\frac{1}{n} \sum_{i=1}^n \sum_{j=1}^n \log \frac{1}{1 + \exp(z_{ij}(-t\hat{g}_i^\top \hat{h}_j + b))}, \quad (2)$$

where $z_{ii} = 1$, $z_{ij} = -1$ if $i \neq j$ and b is a learnable bias term. For classification settings, the SigLIP loss does not provide normalised class conditional probabilities $p(y | \mathbf{x})$ but provides binary classification probabilities. Henceforth, when fine-tuning a SigLIP pre-trained VLM for classification tasks, one typically uses the cross-entropy loss instead.

3.2. Post-hoc Uncertainty Quantification

To estimate predictive uncertainties, we utilise an efficient post-hoc approximation to the Bayesian posterior in conjunction with analytic computation of the uncertainties propagated through the VLM. By using an approximation to the Bayesian posterior over the model parameters, we can estimate uncertainties over the model itself. This, in turn, allows us to obtain uncertainty estimates over the predictions by propagating the model uncertainties through the VLM using our approach. We will now introduce each stage of this procedure step-by-step and discuss how to estimate and propagate uncertainties efficiently. The uncertainty propagation pipeline is illustrated in Fig. 2.

Given a data set of image-text pairs, we aim to estimate the posterior distribution $p(\boldsymbol{\theta} | \mathcal{D})$ of the model parameters of the VLM. Before doing so, let us first consider the

general setting in which a data set $\mathcal{D} = \{(\mathbf{x}_i, \mathbf{y}_i)\}_{i=1}^n$ of input-output tuples is given. In this setting, the posterior distribution over the model parameters $\boldsymbol{\theta}$ is:

$$p(\boldsymbol{\theta} | \mathcal{D}) = \frac{p(\boldsymbol{\theta}) \prod_{(\mathbf{x}, \mathbf{y}) \in \mathcal{D}} p(\mathbf{y} | \mathbf{x}, \boldsymbol{\theta})}{\int_{\boldsymbol{\theta}} p(\boldsymbol{\theta}) \prod_{(\mathbf{x}, \mathbf{y}) \in \mathcal{D}} p(\mathbf{y} | \mathbf{x}, \boldsymbol{\theta}) d\boldsymbol{\theta}} \quad (3)$$

$$= \frac{\text{prior} \times \text{likelihood}}{\text{marginal likelihood}}.$$

Unfortunately, computing the denominator (marginal likelihood) is generally intractable (not feasible) as it requires integration over a high-dimensional space w.r.t. a potentially non-linear function. A classical approach to circumvent this challenge is to approximate the posterior using a Laplace approximation [43], which has recently gained traction in the Bayesian deep learning community [15, 39, 46, 56, 58, 60].

The Laplace approximation hinges on the idea that the posterior distribution is proportional to the joint, *i.e.*,

$$p(\boldsymbol{\theta} | \mathcal{D}) \propto p(\boldsymbol{\theta}, \mathcal{D}) = p(\boldsymbol{\theta}) \prod_{(\mathbf{x}, \mathbf{y}) \in \mathcal{D}} p(\mathbf{y} | \mathbf{x}, \boldsymbol{\theta}) \quad (4)$$

up to an unknown normalisation constant (the marginal likelihood). Moreover, using a second-order Taylor expansion of the log joint around the maximum-a-posteriori (MAP) estimate $\boldsymbol{\theta}_{\text{MAP}}$ (mode of the function) one obtains the unnormalised log density function of a Gaussian centred at $\boldsymbol{\theta}_{\text{MAP}}$, *i.e.*, $\log p(\boldsymbol{\theta}, \mathcal{D}) \approx$

$$\log p(\boldsymbol{\theta}_{\text{MAP}}, \mathcal{D}) - \frac{1}{2}(\boldsymbol{\theta} - \boldsymbol{\theta}_{\text{MAP}})^\top \mathbf{H}(\boldsymbol{\theta} - \boldsymbol{\theta}_{\text{MAP}}), \quad (5)$$

where $\mathbf{H} = (-\nabla^2 \log p(\boldsymbol{\theta}, \mathcal{D})|_{\boldsymbol{\theta}=\boldsymbol{\theta}_{\text{MAP}}})$ is the Hessian matrix of the log joint (prior \times likelihood) at $\boldsymbol{\theta}_{\text{MAP}}$. By matching the marginal likelihood in Eq. (3) with the normalisation constant of a Gaussian, we obtain the Laplace approximation:

$$p(\boldsymbol{\theta} | \mathcal{D}) \approx \mathcal{N}(\boldsymbol{\theta}_{\text{MAP}}, \mathbf{H}^{-1}), \quad (6)$$

with covariance given by the inverse of the Hessian matrix.

In the case of VLMs, the log-likelihood function is defined by the respective loss function, *i.e.*, either the InfoNCE or the SigLIP loss, and the prior arises through the use of an L2 regularisation (weight decay) in the optimisation [53, 74]. Henceforth, we can assume that the model parameters found after pre-training with either loss correspond to a MAP estimate of the posterior distribution. However, to estimate the Laplace approximation of the VLM model parameters, we need to compute the Hessian matrix \mathbf{H} , which is computationally demanding in large-scale models. To resolve this challenge, we leverage a Kronecker-factored Generalized Gauss-Newton (GGN) approximation [45, 56] to the Hessian. Moreover, we apply the Laplace approximation only for the image projection and text projection layers \mathbf{P} and \mathbf{Q} of the

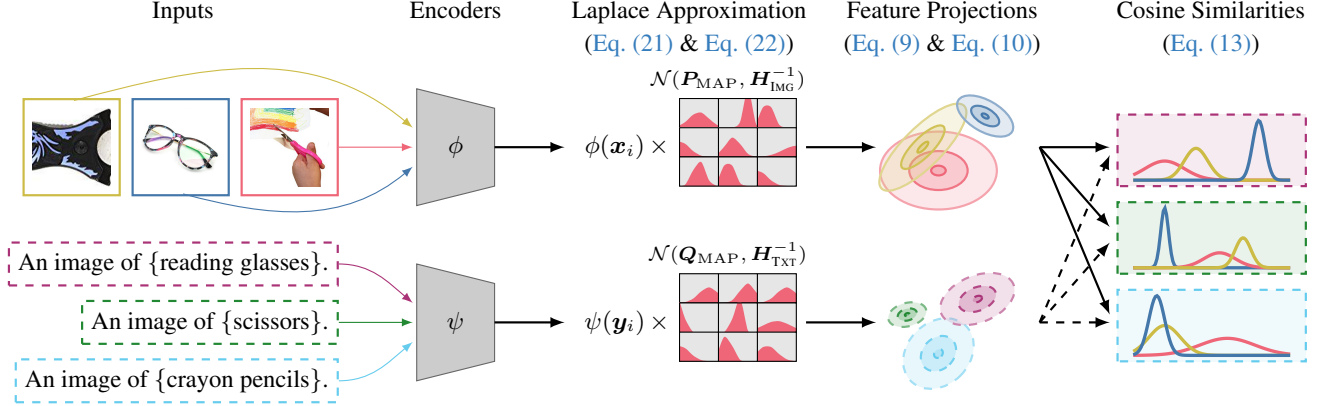


Figure 2. **Illustration of uncertainty propagation in VLMs:** We estimate uncertainties over the last linear layers of both encoders using a Laplace approximation, which induces distributions over the feature projections. We then approximate the distribution over cosine similarities by estimating the expected value and variance accordingly. The cosine similarity distribution is then propagated further to the VLM output.

image and text encoders. Lastly, we assume independence between \mathbf{P} and \mathbf{Q} . The resulting GGN approximations of \mathbf{H}_{IMG} and \mathbf{H}_{TXT} are then given in form of their Kronecker factors \mathbf{A} and \mathbf{B} , *i.e.*,

$$\mathbf{H}_{\text{IMG}} \approx \left(\sqrt{\tau} \mathbf{A}_{\text{IMG}} + \sqrt{\lambda} \mathbf{I} \right) \otimes \left(\sqrt{\tau} \mathbf{B}_{\text{IMG}} + \sqrt{\lambda} \mathbf{I} \right), \quad (7)$$

$$\mathbf{H}_{\text{TXT}} \approx \left(\sqrt{\tau} \mathbf{A}_{\text{TXT}} + \sqrt{\lambda} \mathbf{I} \right) \otimes \left(\sqrt{\tau} \mathbf{B}_{\text{TXT}} + \sqrt{\lambda} \mathbf{I} \right), \quad (8)$$

where $\lambda \geq 0$ is the precision parameter of the prior and $\tau \geq 0$ is a pseudo-data count. The prior precision can be obtained by maximising the marginal likelihood [15, 32] and τ can be optimised additionally [56]. Both parameters can be optimised post-hoc by maximising the marginal likelihood of the Laplace approximation, see App. B for more details. Note that the Kronecker factors \mathbf{A} and \mathbf{B} can be understood as model statistics under the training data, and can be efficiently estimated with automatic differentiation (AD) on a sub-set of the training set.

After having estimated the Laplace approximation to the posterior distribution over \mathbf{P} and \mathbf{Q} , we can analytically compute the distribution over image and text features, respectively. Specifically, we obtain:

$$p(\mathbf{g} \mid \mathcal{D}) = \mathcal{N} \left(\mathbf{g}, \left(\phi(\mathbf{x}^{\text{IMG}})^{\top} \tilde{\mathbf{A}}_{\text{IMG}}^{-1} \phi(\mathbf{x}^{\text{IMG}}) \right) \tilde{\mathbf{B}}_{\text{IMG}}^{-1} \right), \quad (9)$$

$$p(\mathbf{h} \mid \mathcal{D}) = \mathcal{N} \left(\mathbf{h}, \left(\psi(\mathbf{x}^{\text{TXT}})^{\top} \tilde{\mathbf{A}}_{\text{TXT}}^{-1} \psi(\mathbf{x}^{\text{TXT}}) \right) \tilde{\mathbf{B}}_{\text{TXT}}^{-1} \right), \quad (10)$$

where $\tilde{\mathbf{A}}$ and $\tilde{\mathbf{B}}$ denote the Kronecker factors \mathbf{A} and \mathbf{B} containing the prior precision and additional scaling factor.

3.3. Distribution over Cosine Similarities

Given a posterior distribution over the model parameters, evaluating the VLM on an image-text pair will result in the

image and the text feature vectors being *random* vectors instead of deterministically given vectors. Note that the cosine similarity is still well-defined in this setting but is random itself. Hence, we estimate a Gaussian approximation to the distribution over cosine similarities by estimating the first two moments under the distribution over image and text features. Let \mathbf{g} and \mathbf{h} denote random vectors for the image and text embeddings, respectively. Further, let us assume that their distribution follows a Gaussian distribution with mean $\boldsymbol{\mu}_{\mathbf{g}} = (\mu_{g,1}, \dots, \mu_{g,d})$ and $\boldsymbol{\mu}_{\mathbf{h}} = (\mu_{h,1}, \dots, \mu_{h,d})$ and diagonal covariance structure, *i.e.*, $\boldsymbol{\Sigma}_{\mathbf{g}} = \text{diag}(\sigma_{g,1}^2, \dots, \sigma_{g,d}^2)$ and $\boldsymbol{\Sigma}_{\mathbf{h}} = \text{diag}(\sigma_{h,1}^2, \dots, \sigma_{h,d}^2)$.

Given the cosine similarity $S_{\text{Cos}}(\mathbf{x}, \mathbf{y}) = \frac{\mathbf{x}^{\top} \mathbf{y}}{\|\mathbf{x}\| \|\mathbf{y}\|}$ between two vectors, the expected cosine similarity under the distribution of \mathbf{g} and \mathbf{h} is approximately:

$$\mathbb{E}[S_{\text{Cos}}(\mathbf{g}, \mathbf{h})] \approx \frac{\sum_i \mu_{g,i} \mu_{h,i}}{\sqrt{\sum_i \mu_{g,i}^2 + \sigma_{g,i}^2} \sqrt{\sum_i \mu_{h,i}^2 + \sigma_{h,i}^2}}, \quad (11)$$

where we use the fact that $\mathbb{E}[x^2] = \mu_x^2 + \sigma_x^2$ and $\mathbb{E}[\|\mathbf{x}\|] \leq \sqrt{\sum_i \mu_{x,i}^2 + \sigma_{x,i}^2}$ by applying the triangle inequality. We can obtain the second moment (variance) $\text{Var}[S_{\text{Cos}}(\mathbf{g}, \mathbf{h})]$ similarly, which is given as:

$$\text{Var}[S_{\text{Cos}}(\mathbf{g}, \mathbf{h})] = \frac{\sum_i \sigma_{g,i}^2 (\sigma_{h,i}^2 + \mu_{h,i}^2) + \sigma_{h,i}^2 \mu_{g,i}^2}{\sum_i \mu_{g,i}^2 + \sigma_{g,i}^2 \sum_i \mu_{h,i}^2 + \sigma_{h,i}^2}. \quad (12)$$

Henceforth, the local Gaussian approximation to the distribution over cosine similarities is:

$$p(S_{\text{Cos}}(\mathbf{g}, \mathbf{h})) \approx \mathcal{N} \left(\mathbb{E}[S_{\text{Cos}}(\mathbf{g}, \mathbf{h})], \text{Var}[S_{\text{Cos}}(\mathbf{g}, \mathbf{h})] \right). \quad (13)$$

Finally, the predictive distribution $p(y \mid \mathbf{x})$, *e.g.*, in a zero-shot classification setting, is calculated with the probit approximation [20, 21]. Hence, our approach allows for the

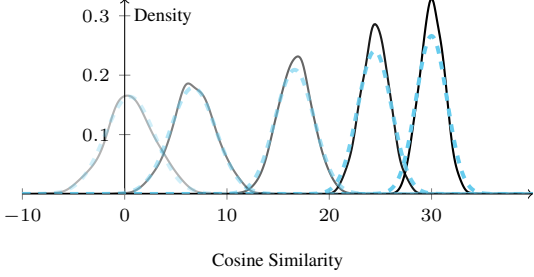


Figure 3. Approximation quality of the Gaussian approximation (---) to the distribution over cosine similarities compared to KDE over samples (—) for image-text pairs with increasing Euclidean distance between their feature projection means (μ_g, μ_h).

direct propagation of model uncertainties to the class conditional. A detailed derivation can be found in App. B.

To empirically assess the approximation quality, we compared the approximation to a kernel density estimate (KDE) over Monte Carlo samples. Fig. 3 illustrates the approximation quality compared to a Monte Carlo simulation for image-text pairs with increasing distance between their feature projection means. We observe that our Gaussian approximation is accurate in the expected value but slightly overestimates the variance in case of high cosine similarity. Further experiment details are given in App. D.

3.4. Probabilistic Active Few-shot Learning

To select the support set on which the VLM is fine-tuned, we utilise acquisition functions from the Bayesian active learning community in conjunction with adaptive target region selection. Let $\mathcal{X}_{\text{test}} = \{\mathbf{x}_i^*\}_{i=1}^{n_{\text{test}}}$ with $\mathbf{x}_i^* \sim p(\mathbf{x}^*)$ be a set of unseen test data (query set) with unknown class labels. Our goal is to find a set $\{(\mathbf{x}_j, y_j)\}_{j=1}^m$ of support candidates of cardinality m with $\mathbf{x}_j, y_j \sim p(\mathbf{x}_j, y_j)$ such that we reduce uncertainty over the class labels of $\mathcal{X}_{\text{test}}$. To approach this problem, we first target the selection process towards the predictive distribution of the query set and then select support set candidates by measuring their influence on the predictive or model uncertainty.

Target Region Selection Inspired by prior work on active learning [44], we first perform k -nearest neighbours (k -NN) selection in the feature space to pre-select support set candidates that are close to the test data. Performing the target region selection has two objectives: (i) targeting the selection towards training data that is potentially relevant for the downstream task, and (ii) reducing the computational overhead for the evaluation of the acquisition functions. As features are not deterministic in our probabilistic model, we either compute the expected cosine similarity (cf., Eq. (11)) or use 2-Wasserstein distance between the image feature distributions (cf., Eq. (9)). Details of the calculation of the Wasserstein distance and k -NN selection are given in App. C.

Acquisition Functions We consider the BALD [19, 26] and EPIG [2] scores as acquisition functions and assess their viability on downstream tasks. Both acquisition functions can utilise model uncertainties estimated by the Laplace approximation, but they differ conceptually in terms of which uncertainties are targeted. Specifically, BALD targets uncertainties over the model parameters, *i.e.*,

$$\text{BALD}(\mathbf{x}) = \mathbb{E}_{p(\boldsymbol{\theta}|\mathcal{D})}[\mathcal{H}(p(y|\mathbf{x}, \mathcal{D})) - \mathcal{H}(p(y|\mathbf{x}, \boldsymbol{\theta}))], \quad (14)$$

where $\mathcal{H}(p(y|\mathbf{x}, \mathcal{D})) = \mathcal{H}(\mathbb{E}_{p(\boldsymbol{\theta}|\mathcal{D})}[p(y|\mathbf{x}, \boldsymbol{\theta})])$ is the entropy of the posterior predictive distribution. Hence, selecting data that maximises the BALD score will maximise the information gained about the true model parameters $\boldsymbol{\theta}$. Different from the BALD score, the EPIG score targets uncertainties in the predictive distribution, *i.e.*,

$$\text{EPIG}(\mathbf{x}) \approx \sum_{i=1}^{n_{\text{test}}} \mathcal{H}(p(y_i^* | \mathbf{x}_i^*), \mathcal{D}) - \mathcal{H}(p(y_i^* | \mathbf{x}_i^*, \mathcal{D} \cup \{(\mathbf{x}, y)\})). \quad (15)$$

Intuitively, the EPIG score measures the expected reduction in predictive uncertainty over the test set when adding \mathbf{x} to the training set. However, to compute the EPIG score, one needs to estimate the entropy of the posterior predictive distribution after including \mathbf{x} in the training set.

Online Laplace Approximation We use an online Laplace approximation to efficiently update the posterior. Specifically, given the current Laplace approximation of the posterior over the image projection matrix \mathbf{P} , we update the posterior distribution by updating the matrix \mathbf{P} using a gradient step and updating the Kronecker factors accordingly. In particular, at the $t + 1$ th step with support set candidate $\mathbf{x}_{t+1}^{\text{IMG}}$ we perform the following updates:

$$\mathbf{P}_{t+1} = \mathbf{P}_t - \gamma \nabla_{\mathbf{P}} \mathcal{L}(\mathbf{x}_{t+1}^{\text{IMG}}, \mathbf{X}^{\text{TXT}}), \quad (16)$$

$$\mathbf{A}_{\text{IMG}, t+1} = \frac{(n+t)\mathbf{A}_{\text{IMG}, t} + \beta \mathbf{A}_{\mathbf{x}_{t+1}}}{n+t+1}, \quad (17)$$

$$\mathbf{B}_{\text{IMG}, t+1} = \frac{(n+t)\mathbf{B}_{\text{IMG}, t} + \beta \mathbf{B}_{\mathbf{x}_{t+1}}}{n+t+1}, \quad (18)$$

where $\gamma \geq 0$ and $\beta \geq 0$ are hyperparameters and

$$\mathbf{A}_{\mathbf{x}_{t+1}} = \phi(\mathbf{x}_{t+1}^{\text{IMG}}) \phi(\mathbf{x}_{t+1}^{\text{IMG}})^{\top}, \quad (19)$$

$$\mathbf{B}_{\mathbf{x}_{t+1}} = \mathbf{J}_{\text{IMG}}(\mathbf{x}_{t+1}^{\text{IMG}})^{\top} \boldsymbol{\Lambda}_{\text{IMG}} \mathbf{J}_{\text{IMG}}(\mathbf{x}_{t+1}^{\text{IMG}}), \quad (20)$$

denote the factors for observation $\mathbf{x}_{t+1}^{\text{IMG}}$ with $\mathbf{J}(\cdot)$ being the Jacobian and $\boldsymbol{\Lambda}$ the Hessian of the likelihood function w.r.t. the logits. In the case of the InfoNCE loss, $\boldsymbol{\Lambda}$ is the Hessian matrix of the respective softmax function used in InfoNCE. For SigLIP, on the other hand, $\boldsymbol{\Lambda}$ is the Hessian matrix of the binary classification loss in Eq. (42). In addition, one can re-fit the prior precision after each update set, as commonly

Table 1. **Zero-shot Results:** Quantitative evaluation of uncertainty estimation across multiple data sets in the zero-shot setting for the OpenCLIP ViT-B-32 model. Our proposed BayesVLM consistently outperforms baseline methods across accuracy (ACC, in %), negative log predictive density (NLPD), and expected calibration error (ECE, in %) metrics.

Metrics	Methods	FLOWERS-102	FOOD-101	EUROSAT	CIFAR-100	DTD
ACC \uparrow	CLIP [53]	68.99 \pm 0.59	80.21 \pm 0.25	35.25 \pm 0.53	73.76 \pm 0.44	53.24 \pm 1.15
	CLIP (temp. scaling)	68.99 \pm 0.59	80.21 \pm 0.25	35.25 \pm 0.53	73.76 \pm 0.44	53.24 \pm 1.15
	PCME++ [9]	40.59 \pm 0.63	65.47 \pm 0.30	28.83 \pm 0.50	42.52 \pm 0.49	23.30 \pm 0.97
	PCME++ (Eq. (13))	40.43 \pm 0.63	65.54 \pm 0.30	28.83 \pm 0.50	42.60 \pm 0.49	23.19 \pm 0.97
	BayesVLM	68.95 \pm 0.59	80.57 \pm 0.25	36.48 \pm 0.53	73.79 \pm 0.44	52.77 \pm 1.15
NLPD \downarrow	CLIP [53]	1.90 \pm 0.05	0.70 \pm 0.01	2.16 \pm 0.02	0.97 \pm 0.02	1.85 \pm 0.05
	CLIP (temp. scaling)	1.80 \pm 0.04	0.68 \pm 0.01	2.01 \pm 0.02	0.94 \pm 0.02	1.76 \pm 0.04
	PCME++ [9]	3.22 \pm 0.05	1.30 \pm 0.01	3.53 \pm 0.03	2.28 \pm 0.02	4.05 \pm 0.07
	PCME++ (Eq. (13))	3.04 \pm 0.04	1.25 \pm 0.01	3.19 \pm 0.03	2.21 \pm 0.02	3.74 \pm 0.06
	BayesVLM	1.76 \pm 0.04	0.68 \pm 0.01	1.90 \pm 0.02	0.95 \pm 0.02	1.78 \pm 0.04
ECE \downarrow	CLIP [53]	6.59	3.91	35.40	6.31	15.32
	CLIP (temp. scaling)	3.79	1.37	31.74	3.47	10.89
	PCME++ [9]	8.81	6.78	34.87	10.78	25.95
	PCME++ (Eq. (13))	2.79	1.54	30.58	4.89	19.18
	BayesVLM	3.95	0.79	28.16	2.69	10.25

Table 2. **Zero-shot Results:** Quantitative evaluation of uncertainty estimation across multiple data sets in the zero-shot setting for the SigLIP-B-16 model. Our proposed BayesVLM performs better or on par with baseline methods across accuracy (ACC, in %), negative log predictive density (NLPD), and expected calibration error (ECE, in %) metrics.

Metrics	Methods	FLOWERS-102	FOOD-101	EUROSAT	CIFAR-100	DTD
ACC \uparrow	SigLIP [74]	82.31 \pm 0.49	88.81 \pm 0.20	40.74 \pm 0.55	71.27 \pm 0.45	63.62 \pm 1.11
	SigLIP (temp. scaling)	82.31 \pm 0.49	88.81 \pm 0.20	40.74 \pm 0.55	71.27 \pm 0.45	63.62 \pm 1.11
	BayesVLM	82.40 \pm 0.49	88.87 \pm 0.20	40.72 \pm 0.55	71.22 \pm 0.45	63.67 \pm 1.11
NLPD \downarrow	SigLIP [74]	0.88 \pm 0.03	0.38 \pm 0.01	1.98 \pm 0.02	1.08 \pm 0.02	1.48 \pm 0.05
	SigLIP (temp. scaling)	1.91 \pm 0.01	1.64 \pm 0.00	1.86 \pm 0.01	2.38 \pm 0.01	2.20 \pm 0.02
	BayesVLM	0.86 \pm 0.03	0.38 \pm 0.01	1.95 \pm 0.02	1.08 \pm 0.02	1.46 \pm 0.05
ECE \downarrow	SigLIP [74]	4.31	1.66	15.95	1.97	8.19
	SigLIP (temp. scaling)	62.79	65.83	16.90	57.79	46.50
	BayesVLM	4.49	2.65	15.08	1.72	6.61

done in online Laplace [32, 40]. The updated posterior is then obtained by application of Eq. (21). Further technical details are given in App. B.

4. Experiments

To assess the viability of our approach, we performed a series of experiments to evaluate the quality and calibration of post-hoc uncertainty estimates, the use of post-hoc uncertainties for active learning, and a qualitative assessment of the distribution over cosine similarities. We evaluated the performance of uncertainty quantification and calibration in the zero-shot classification setting on common benchmark data sets (Flowers-102 [49], Food-101 [4], EuroSAT [23], CIFAR-100 [36], and DTD [12]) on the OpenCLIP [31, 61] ViT-B-32 model and SigLIP-B-16 model [74]. The experiments for active learning are conducted on OpenCLIP ViT-B-32 and done in the cross-domain setting for OfficeHome [69] and ImageNet variants (ImageNet-R [24] and ImageNet-Sketch

[70]). In addition, we present a qualitative assessment of the distribution over cosine similarities for a datum from the OfficeHome data set. In all experiments, we estimated the Hessian of the Laplace approximation using a randomly sampled subset consisting of 30k image-text pairs from the LAION-400M data set [61]. We report the accuracy (ACC), the negative log predictive likelihood (NLPD), and the expected calibration error (ECE) to assess the performance of each method. When reporting the results, we use a paired *t*-test with $p = 0.05$ to bold results with a significant statistical difference. We provide further experimental details and additional results in App. D and App. E, respectively.

4.1. Uncertainty Quantification and Calibration

We evaluated the quality and calibration of uncertainty estimates obtained by our (BayesVLM) post-hoc strategy on zero-shot settings. For the CLIP [31] model, we compare against vanilla CLIP, CLIP with temperature scaling [22, 50],

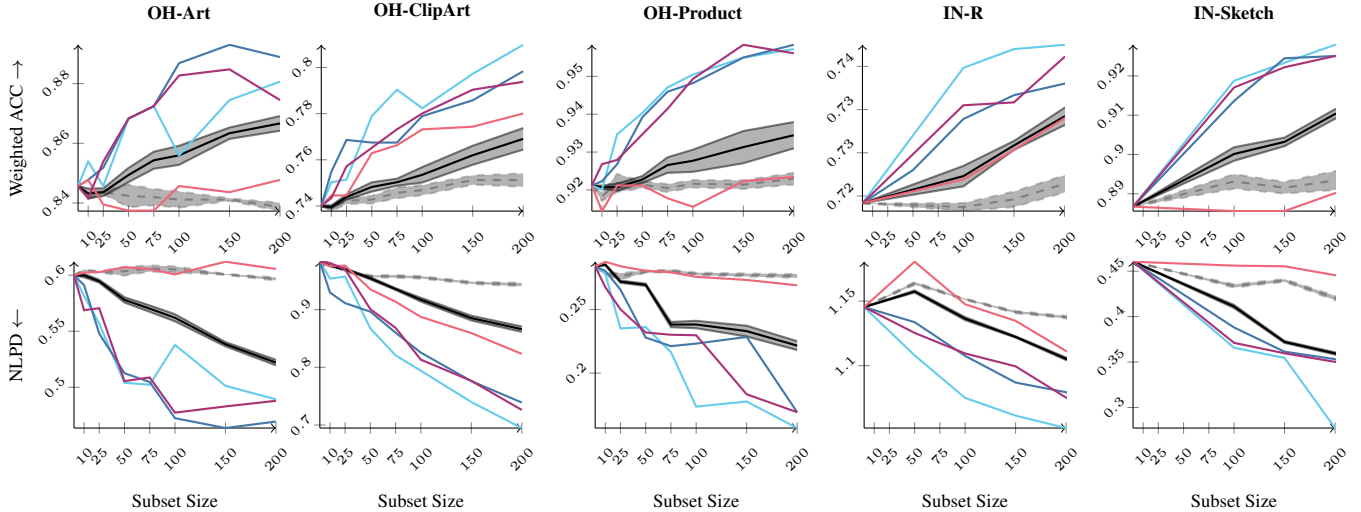


Figure 4. **Active Learning Results:** We present results for EPIG (—●—), BALD (—■—), Entropy (targeted) (—▲—), Entropy (—◆—), Random selection (targeted) (—×—), Random selection (— —) on the OfficeHome data set (OH) and ImageNet variants (IN). We observe that active learning based on our post-hoc uncertainties consistently improves upon random and entropy-based selection.

PCME++ [9], and PCME++ with our approximation to the distribution over cosine similarities in Sec. 3.3. For SigLIP [74], we compare against vanilla SigLIP and SigLIP with temperature scaling [22, 50]. The hyperparameters have been optimised on a random subset of ImageNet consisting of 100 classes and 1097 test data points in total as a proxy. In particular, the temperature scale for CLIP and SigLIP with temperature scaling was selected by minimising the negative log predictive density (NLPD) on the ImageNet proxy. For BayesVLM, we estimated the pseudo-data count τ using a grid search over values in $\tau \in [1, 5, 10, 15, \dots, 50]$ and optimised the prior precision based on the marginal likelihood (on LAION-400M) for each τ . We report the results for the pseudo-data count that achieved the highest NLPD on the ImageNet proxy. For PCME++, we used the CLIP ViT-B/16 checkpoint provided by the authors with uncertainty adapter trained on CC-3M [63], CC-12M [7], and Redcaps [16].

Table 1 shows the mean and standard error computed over the test set of the respective data set for CLIP-based models. We observe that BayesVLM provides improvements in terms of ACC, NLPD, and ECE over CLIP in all cases. Moreover, BayesVLM provides on-par or better results than temperature scaling and PCME++. In addition, we find that our approximation of the cosine similarity consistently improves the NLPD and ECE of PCME++, illustrating its versatility. For instance, for Food-101, the ECE reduces from 6.78% to 1.54% for PCME++, with BayesVLM providing an ECE of 0.79%. Table 2 shows the mean and standard error computed over the test set of the respective data set for SigLIP-based models. As SigLIP is not trained on the LAION-400M data set, the training data set and the data set we used to estimate its Hessian are mismatched. This mismatch results in a large

τ that pushes the posterior towards the MAP estimation, potentially degenerating the performance of BayesVLM. We observe that on Flowers-102 and Food-101, BayesVLM has higher ECE compared to SigLIP, and for the rest of the data sets, BayesVLM provides improvements in terms of ACC, NLPD, and ECE over SigLIP. Note that we found that temperature scaling degenerates the performance of SigLIP in most cases for NLPD and ECE. Overall, we observe that BayesVLM improves model calibration and uncertainty estimation without compromising performance, indicating the effectiveness of our post-hoc strategy.

4.2. Probabilistic Active Learning

We conducted experiments in an active learning setting to further assess the utility of our uncertainty estimates. For this, we constructed one task for each domain in the OfficeHome [69] data set. Each task consists of the test data points for the respective domain, and the potential training data candidates are across all domains in OfficeHome, making the experiments cross-domain. In addition, we performed a similar study on ImageNet variants (ImageNet-R and ImageNet-Sketch) to illustrate the approach’s scalability. In the active learning setting, the goal is to select an informative support set of fixed cardinality (subset size) on which to fine-tune the CLIP model. We incorporate our uncertainty estimates into the acquisition functions BALD and EPIG (see Sec. 3.4), and compare against random selection on the training data (random), random selection on the test data followed by 1-NN selection of training samples (random targeted), entropy-based selection combined with/without 1-NN selection (entropy targeted/entropy). We selected the pseudo-data count as described in Sec. 3.2 and learned the

prior precision by maximising the marginal likelihood. See App. D and App. E for more details and results on SigLIP.

As shown in Fig. 4, we find that incorporating post-hoc uncertainties into the selection process consistently improves upon entropy-based selection and random selection. We also observe that targeted support set selection improves the performance, as indicated by the performance gap between ‘random’ and ‘random targeted’.

4.3. Interpreting Probabilistic Cosine Similarities

We performed a qualitative assessment of the resulting distribution over cosine similarities. For this, we randomly picked a test example from the OfficeHome clipart domain and evaluated the expected value and variance of the cosine similarity under increasing amounts of corruption in both the image and text domains. In particular, for the text domain, we randomly replace characters with ‘x’ characters in the input string. For the image domain, we randomly add grey squares to the input image. The pseudo-data count was set based on the approach described in Sec. 4.1 with prior precision learning via the marginal likelihood. Fig. 5 shows the expected value and the variance of the cosine similarity for each corruption pair. We observe that the expected cosine similarity decreases with an increasing amount of corruption in the text and/or image domain. Moreover, we see that the variance of the cosine similarity steadily increases with the amount of corruption. Note that we observe a slight increase in the cosine similarity after one character has been replaced, indicating that performing predictions solely on the expected cosine similarity can be problematic. In this case, the variance over cosine similarities can capture the change in the input, highlighting the importance of capturing and propagating the model uncertainties.

5. Discussion and Conclusion

In this work, we introduced a novel approach for post-hoc uncertainty estimation and propagation for large-scale vision language models (VLMs) like CLIP [53] and SigLIP [74]. For this, we proposed utilizing a post-hoc approximation to the posterior over the last layer of each encoder of the VLM and derive an analytic form of an approximate distribution over cosine similarities. This allows us to estimate uncertainties over the model and the predictions without any architectural changes. The uncertainties over the logits are computed through a novel local Gaussian approximation and propagated to the predictive distribution using the probit approximation. On common zero-shot classification benchmarks, we demonstrate that our post-hoc uncertainty estimation technique provides well-calibrated uncertainties and consistent improvements in negative log predictive density (NLPD) and expected calibration error (ECE), over CLIP and SigLIP. We further found improvements in NLPD and

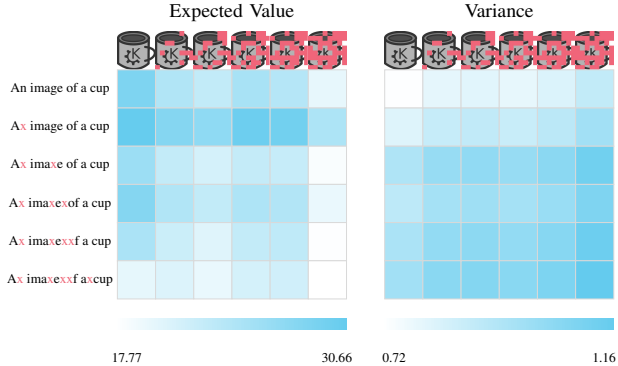


Figure 5. Illustration of the distribution over cosine similarities, depicting expected value and variance, for varying image and text corruptions. The expected cosine similarity decreases with increasing levels of corruption while the variance steadily increases. This shows that our approximation to the distribution over cosine similarities captures model uncertainties in out-of-distribution settings.

ECE over temperature-scaled CLIP without the need for additional temperature scaling.

To showcase the efficacy of the uncertainties estimated obtained through our method (BayesVLM), we conducted additional experiments in the active learning setting and provided a qualitative assessment of the distribution over cosine similarities. For this, we conducted experiments in the cross-domain setting evaluated on OfficeHome [69] and ImageNet variants (ImageNet-R and ImageNet-Sketch). We discussed the two acquisition functions based on model uncertainties and compared those against common baselines. We presented a targeted selection based on k -nearest neighbours to improve the scalability of the approach and target the selection process towards relevant regions in the input space. We showed that targeted selection improves results and that incorporating uncertainties further improves results.

Limitations Our current approach requires estimating the Hessian matrix from the original training data. However, for many large-scale VLMs, the training data is closed-source, and we had to resort to the LAION data set as a proxy for our SigLIP experiments, resulting in a likely degeneration of the Hessian estimate. We aim to further investigate the side effects of estimating the Hessian based on a proxy data set and possible solutions to improve the estimation result, *e.g.*, by considering the Jacobian term in the second-order Taylor expansion of the log joint. Our experimental results are currently limited to a small subset of VLMs and limited to models trained using a matching loss function. In the future, we aim to extend our approach to generative VLMs [8, 42, 65] to enable post-hoc uncertainty estimation and propagation in, *e.g.*, text generation settings.

Reproducibility The code for the experiments is available at: <https://aaltoml.github.io/BayesVLM/>.

Acknowledgements

AS, RL, and SM acknowledge funding from the Research Council of Finland (grant number 339730). MT acknowledges funding from the Research Council of Finland (grant number 347279). MK and SM acknowledge funding from the Finnish Center for Artificial Intelligence (FCAI). SK and ZA acknowledge partial funding by the ERC (853489 - DEXIM) and the Alfried Krupp von Bohlen und Halbach Foundation. SK thanks the International Max Planck Research School for Intelligent Systems (IMPRS-IS). We acknowledge CSC – IT Center for Science, Finland, for awarding this project access to the LUMI supercomputer, owned by the EuroHPC Joint Undertaking, hosted by CSC (Finland) and the LUMI consortium through CSC. We acknowledge the computational resources provided by the Aalto Science-IT project. Finally, we thank Riccardo Mereu for providing feedback on the manuscript.

References

- [1] Jihwan Bang, Sumyeong Ahn, and Jae-Gil Lee. Active prompt learning in vision language models. In *Proceedings of the IEEE/CVF Conference on Computer Vision and Pattern Recognition*, pages 27004–27014, 2024. 1, 2
- [2] Freddie Bickford Smith, Andreas Kirsch, Sebastian Farquhar, Yarin Gal, Adam Foster, and Tom Rainforth. Prediction-oriented Bayesian active learning. In *International Conference on Artificial Intelligence and Statistics*, 2023. 2, 5, 17
- [3] Rishi Bommasani, Drew A Hudson, Ehsan Adeli, Russ Altman, Simran Arora, Sydney von Arx, Michael S Bernstein, Jeannette Bohg, Antoine Bosselut, Emma Brunskill, et al. On the opportunities and risks of foundation models. *arXiv preprint arXiv:2108.07258*, 2021. 1
- [4] Lukas Bossard, Matthieu Guillaumin, and Luc Van Gool. Food-101 - mining discriminative components with random forests. In *European Conference on Computer Vision*. Springer, 2014. 6
- [5] Klaus Brinker. Incorporating diversity in active learning with support vector machines. In *International conference on Machine Learning (ICML)*, 2003. 1
- [6] Tom Brown, Benjamin Mann, Nick Ryder, Melanie Subbiah, Jared D Kaplan, Prafulla Dhariwal, Arvind Neelakantan, Pranav Shyam, Girish Sastry, Amanda Askell, et al. Language models are few-shot learners. *Advances in Neural Information Processing Systems*, 33:1877–1901, 2020. 1
- [7] Soravit Changpinyo, Piyush Sharma, Nan Ding, and Radu Soricut. Conceptual 12M: Pushing web-scale image-text pre-training to recognize long-tail visual concepts. In *Proceedings of the IEEE Conference on Computer Vision and Pattern Recognition*, 2021. 7
- [8] Zhe Chen, Jiannan Wu, Wenhai Wang, Weijie Su, Guo Chen, Sen Xing, Muyan Zhong, Qinglong Zhang, Xizhou Zhu, Lewei Lu, Bin Li, Ping Luo, Tong Lu, Yu Qiao, and Jifeng Dai. Internvl: Scaling up vision foundation models and aligning for generic visual-linguistic tasks. *arXiv preprint arXiv:2312.14238*, 2023. 8
- [9] Sanghyuk Chun. Improved probabilistic image-text representations. In *International Conference on Learning Representations*, 2024. 2, 6, 7
- [10] Sanghyuk Chun, Seong Joon Oh, Rafael Sampaio De Rezende, Yannis Kalantidis, and Diane Larlus. Probabilistic embeddings for cross-modal retrieval. In *Proceedings of the IEEE/CVF Conference on Computer Vision and Pattern Recognition*, pages 8415–8424, 2021. 1, 2
- [11] Sanghyuk Chun, Wonjae Kim, Song Park, and Sangdoon Yun. Probabilistic language-image pre-training. *arXiv preprint arXiv:2410.18857*, 2024. 1, 2
- [12] M. Cimpoi, S. Maji, I. Kokkinos, S. Mohamed, , and A. Vedaldi. Describing textures in the wild. In *Proceedings of the IEEE Conference on Computer Vision and Pattern Recognition*, 2014. 6
- [13] David A Cohn, Zoubin Ghahramani, and Michael I Jordan. Active learning with statistical models. *Journal of Artificial Intelligence Research*, 1996. 1
- [14] Sanjoy Dasgupta. Two faces of active learning. *Theoretical Computer Science*, 412(19):1767–1781, 2011. 1
- [15] Erik Daxberger, Agustinus Kristiadi, Alexander Immer, Runa Eschenhagen, Matthias Bauer, and Philipp Hennig. Laplace redux-effortless bayesian deep learning. *Advances in Neural Information Processing Systems*, 34:20089–20103, 2021. 3, 4, 17
- [16] Karan Desai, Gaurav Kaul, Zubin Aysola, and Justin Johnson. Redcaps: Web-curated image-text data created by the people, for the people. *arXiv preprint arXiv:2111.11431*, 2021. 7
- [17] Jacob Devlin, Ming-Wei Chang, Kenton Lee, and Kristina Toutanova. BERT: Pre-training of deep bidirectional transformers for language understanding. In *Proceedings of the 2019 Conference of the North American Chapter of the Association for Computational Linguistics: Human Language Technologies, Volume 1 (Long and Short Papers)*. Association for Computational Linguistics, 2019. 1
- [18] Samir Yitzhak Gadre, Gabriel Ilharco, Alex Fang, Jonathan Hayase, Georgios Smyrnis, Thao Nguyen, Ryan Marten, Mitchell Wortsman, Dhruva Ghosh, Jieyu Zhang, et al. Datacomp: In search of the next generation of multimodal datasets. *Advances in Neural Information Processing Systems*, 2023. 2
- [19] Yarin Gal, Riashat Islam, and Zoubin Ghahramani. Deep bayesian active learning with image data. In *International Conference on Machine Learning*, pages 1183–1192, 2017. 2, 5
- [20] Indrayudh Ghosal, Yunzhe Zhou, and Giles Hooker. The infinitesimal jackknife and combinations of models. *arXiv preprint arXiv:2209.00147*, 2022. 4
- [21] Mark N Gibbs. *Bayesian Gaussian processes for regression and classification*. PhD thesis, University of Glasgow, 1998. 4
- [22] Chuan Guo, Geoff Pleiss, Yu Sun, and Kilian Q Weinberger. On calibration of modern neural networks. In *International conference on machine learning*, pages 1321–1330, 2017. 6, 7
- [23] Patrick Helber, Benjamin Bischke, Andreas Dengel, and Damian Borth. Eurosat: A novel dataset and deep learning benchmark for land use and land cover classification. *IEEE*

- Journal of Selected Topics in Applied Earth Observations and Remote Sensing*, 12(7), 2019. 6
- [24] Dan Hendrycks, Steven Basart, Norman Mu, Saurav Kadavath, Frank Wang, Evan Dorundo, Rahul Desai, Tyler Zhu, Samyak Parajuli, Mike Guo, Dawn Song, Jacob Steinhardt, and Justin Gilmer. The many faces of robustness: A critical analysis of out-of-distribution generalization. In *Proceedings of the IEEE/CVF International Conference on Computer Vision*. IEEE, 2021. 6, 18
- [25] Alex Holub, Pietro Perona, and Michael C Burl. Entropy-based active learning for object recognition. In *Proceedings of the IEEE/CVF Conference on Computer Vision and Pattern Recognition Workshops*, pages 1–8. IEEE, 2008. 2
- [26] Neil Houlsby, Ferenc Huszár, Zoubin Ghahramani, and Máté Lengyel. Bayesian active learning for classification and preference learning. *arXiv preprint arXiv:1112.5745*, 2011. 2, 5, 16, 17
- [27] Shell Xu Hu, Da Li, Jan Stühmer, Minyoung Kim, and Timothy M Hospedales. Pushing the limits of simple pipelines for few-shot learning: External data and fine-tuning make a difference. In *Proceedings of the IEEE/CVF Conference on Computer Vision and Pattern Recognition*, pages 9068–9077, 2022. 1
- [28] Jonas Hübner, Bhavya Sukhija, Lenart Treven, Yarden As, and Andreas Krause. Active few-shot fine-tuning. *arXiv preprint arXiv:2402.15441*, 2024. 1
- [29] Jonas Hübner, Sascha Bongni, Ido Hakimi, and Andreas Krause. Efficiently learning at test-time: Active fine-tuning of LLMs. *arXiv preprint arXiv:2410.08020*, 2024.
- [30] Jonas Hübner, Bhavya Sukhija, Lenart Treven, Yarden As, and Andreas Krause. Transductive active learning: Theory and applications. *arXiv preprint arXiv:2402.15898*, 2024. 1
- [31] Gabriel Ilharco, Mitchell Wortsman, Ross Wightman, Cade Gordon, Nicholas Carlini, Rohan Taori, Achal Dave, Vaishaal Shankar, Hongseok Namkoong, John Miller, Hannaneh Hajishirzi, Ali Farhadi, and Ludwig Schmidt. Openclip, 2021. 6
- [32] Alexander Immer, Matthias Bauer, Vincent Fortuin, Gunnar Rätsch, and Khan Mohammad Emtiyaz. Scalable marginal likelihood estimation for model selection in deep learning. In *International Conference on Machine Learning*, pages 4563–4573, 2021. 4, 6, 13
- [33] Yatai Ji, Junjie Wang, Yuan Gong, Lin Zhang, Yanru Zhu, Hongfa Wang, Jiaying Zhang, Tetsuya Sakai, and Yujia Yang. Map: Multimodal uncertainty-aware vision-language pre-training model. In *Proceedings of the IEEE/CVF Conference on Computer Vision and Pattern Recognition*, pages 23262–23271, 2023. 2
- [34] Menglin Jia, Luming Tang, Bor-Chun Chen, Claire Cardie, Serge Belongie, Bharath Hariharan, and Ser-Nam Lim. Visual prompt tuning. In *European Conference on Computer Vision*, pages 709–727. Springer, 2022. 1
- [35] Shyamgopal Karthik, Karsten Roth, Massimiliano Mancini, and Zeynep Akata. Vision-by-language for training-free compositional image retrieval. In *International Conference on Learning Representations*, 2024. 2
- [36] Alex Krizhevsky and Geoffrey Hinton. Learning multiple layers of features from tiny images. Technical report, University of Toronto, 2009. 6
- [37] David D Lewis and Jason Catlett. Heterogeneous uncertainty sampling for supervised learning. In *Machine Learning Proceedings*. Elsevier, 1994. 1
- [38] Hao Li, Jingkuan Song, Lianli Gao, Pengpeng Zeng, Haonan Zhang, and Gongfu Li. A differentiable semantic metric approximation in probabilistic embedding for cross-modal retrieval. *Advances in Neural Information Processing Systems*, 35:11934–11946, 2022. 2
- [39] Rui Li, Marcus Klasson, Arno Solin, and Martin Trapp. Streamlining prediction in bayesian deep learning. *arXiv preprint arXiv:2411.18425*, 2024. 3
- [40] Jihao Andreas Lin, Javier Antorán, and José Miguel Hernández-Lobato. Online laplace model selection revisited. *arXiv preprint arXiv:2307.06093*, 2023. 6
- [41] Zhiqiu Lin, Samuel Yu, Zhiyi Kuang, Deepak Pathak, and Deva Ramanan. Multimodality helps unimodality: Cross-modal few-shot learning with multimodal models. In *Proceedings of the IEEE/CVF Conference on Computer Vision and Pattern Recognition*, pages 19325–19337, 2023. 1
- [42] Haotian Liu, Chunyuan Li, Qingyang Wu, and Yong Jae Lee. Visual instruction tuning. In *Advances in Neural Information Processing Systems*, 2023. 8
- [43] David JC MacKay. Information-based objective functions for active data selection. *Neural Computation*, 1992. 1, 3
- [44] Katerina Margatina, Giorgos Vernikos, Loïc Barrault, and Nikolaos Aletras. Active learning by acquiring contrastive examples. In *Proceedings of the 2021 Conference on Empirical Methods in Natural Language Processing*. Association for Computational Linguistics, 2021. 2, 5
- [45] James Martens and Roger Grosse. Optimizing neural networks with kronecker-factored approximate curvature. In *International conference on Machine Learning*, pages 2408–2417, 2015. 3
- [46] Lassi Meronen, Martin Trapp, Andrea Pilzer, Le Yang, and Arno Solin. Fixing overconfidence in dynamic neural networks. In *IEEE/CVF Winter Conference on Applications of Computer Vision*, pages 2680–2690, 2024. 3
- [47] Thomas Müller, Guillermo Pérez-Torró, Angelo Basile, and Marc Franco-Salvador. Active few-shot learning with fasl. In *International Conference on Applications of Natural Language to Information Systems*, 2022. 1
- [48] Andrei Neculai, Yanbei Chen, and Zeynep Akata. Probabilistic compositional embeddings for multimodal image retrieval. In *Proceedings of the IEEE/CVF Conference on Computer Vision and Pattern Recognition Workshops*, 2022. 2
- [49] Maria-Elena Nilsback and Andrew Zisserman. Automated flower classification over a large number of classes. In *Indian Conference on Computer Vision, Graphics and Image Processing*, 2008. 6
- [50] Jeremy Nixon, Michael W Dusenberry, Linchuan Zhang, Ghassen Jerfel, and Dustin Tran. Measuring calibration in deep learning. In *Proceedings of the IEEE/CVF Conference on Computer Vision and Pattern Recognition Workshops*, 2019. 6, 7

- [51] Aaron van den Oord, Yazhe Li, and Oriol Vinyals. Representation learning with contrastive predictive coding. *arXiv preprint arXiv:1807.03748*, 2018. 3
- [52] Dustin Podell, Zion English, Kyle Lacey, Andreas Blattmann, Tim Dockhorn, Jonas Müller, Joe Penna, and Robin Rombach. Sdxl: Improving latent diffusion models for high-resolution image synthesis. *arXiv preprint arXiv:2307.01952*, 2023. 2
- [53] Alec Radford, Jong Wook Kim, Chris Hallacy, Aditya Ramesh, Gabriel Goh, Sandhini Agarwal, Girish Sastry, Amanda Askell, Pamela Mishkin, Jack Clark, et al. Learning transferable visual models from natural language supervision. In *International Conference on Machine Learning*, pages 8748–8763, 2021. 1, 2, 3, 6, 8
- [54] Carl Edward Rasmussen and Christopher K. I. Williams. *Gaussian Processes for Machine Learning*. The MIT Press, 2006. 14
- [55] Pengzhen Ren, Yun Xiao, Xiaojun Chang, Po-Yao Huang, Zhihui Li, Brij B Gupta, Xiaojiang Chen, and Xin Wang. A survey of deep active learning. *ACM Computing Surveys*, 2021. 2
- [56] Hippolyt Ritter, Aleksandar Botev, and David Barber. A scalable laplace approximation for neural networks. In *International Conference on Learning Representations*, 2018. 3, 4, 18
- [57] Robin Rombach, Andreas Blattmann, Dominik Lorenz, Patrick Esser, and Björn Ommer. High-resolution image synthesis with latent diffusion models. In *Proceedings of the IEEE/CVF Conference on Computer Vision and Pattern Recognition*, 2022. 2
- [58] Subhankar Roy, Martin Trapp, Andrea Pilzer, Juho Kannala, Nicu Sebe, Elisa Ricci, and Arno Solin. Uncertainty-guided source-free domain adaptation. In *European Conference on Computer Vision*, pages 537–555. Springer, 2022. 3
- [59] Kuniaki Saito, Kihyuk Sohn, Xiang Zhang, Chun-Liang Li, Chen-Yu Lee, Kate Saenko, and Tomas Pfister. Pic2word: Mapping pictures to words for zero-shot composed image retrieval. In *Proceedings of the IEEE/CVF Conference on Computer Vision and Pattern Recognition*, 2023. 2
- [60] Aidan Scannell, Riccardo Mereu, Paul Edmund Chang, Ella Tamir, Joni Pajarinen, and Arno Solin. Function-space parameterization of neural networks for sequential learning. In *International Conference on Learning Representations*, 2024. 3
- [61] Christoph Schuhmann, Romain Beaumont, Richard Vencu, Cade Gordon, Ross Wightman, Mehdi Cherti, Theo Coombes, Aarush Katta, Clayton Mullis, Mitchell Wortsman, et al. Laion-5b: An open large-scale dataset for training next generation image-text models. *Advances in Neural Information Processing Systems*, 35:25278–25294, 2022. 1, 2, 6, 18
- [62] Ozan Sener and Silvio Savarese. Active learning for convolutional neural networks: A core-set approach. In *International Conference on Learning Representations*, 2018. 2
- [63] Piyush Sharma, Nan Ding, Sebastian Goodman, and Radu Soricut. Conceptual captions: A cleaned, hypernymed, image alt-text dataset for automatic image captioning. In *Proceedings of ACL*, 2018. 7
- [64] Julio Silva-Rodriguez, Sina Hajimiri, Ismail Ben Ayed, and Jose Dolz. A closer look at the few-shot adaptation of large vision-language models. In *Proceedings of the IEEE/CVF Conference on Computer Vision and Pattern Recognition*, pages 23681–23690, 2024. 1
- [65] Shengbang Tong, Ellis Brown, Penghao Wu, Sanghyun Woo, Manoj Middepogu, Sai Charitha Akula, Jihan Yang, Shusheng Yang, Adithya Iyer, Xichen Pan, et al. Cambrian-1: A fully open, vision-centric exploration of multimodal LLMs. *arXiv preprint arXiv:2406.16860*, 2024. 8
- [66] Hugo Touvron, Thibaut Lavril, Gautier Izacard, Xavier Martinet, Marie-Anne Lachaux, Timothée Lacroix, Baptiste Rozière, Naman Goyal, Eric Hambro, Faisal Azhar, et al. Llama: Open and efficient foundation language models. *arXiv preprint arXiv:2302.13971*, 2023. 1
- [67] Weijie Tu, Weijian Deng, Dylan Campbell, Stephen Gould, and Tom Gedeon. An empirical study into what matters for calibrating vision-language models. In *ICML*, 2024. 2
- [68] Uddeshya Upadhyay, Shyamgopal Karthik, Massimiliano Mancini, and Zeynep Akata. Problvm: Probabilistic adapter for frozen vision-language models. In *Proceedings of the IEEE/CVF International Conference on Computer Vision*, pages 1899–1910, 2023. 1, 2
- [69] Hemanth Venkateswara, Jose Eusebio, Shayok Chakraborty, and Sethuraman Panchanathan. Deep hashing network for unsupervised domain adaptation. In *Proceedings of the IEEE Conference on Computer Vision and Pattern Recognition*, pages 5018–5027, 2017. 6, 7, 8, 18
- [70] Haohan Wang, Songwei Ge, Zachary Lipton, and Eric P Xing. Learning robust global representations by penalizing local predictive power. In *Advances in Neural Information Processing Systems*, pages 10506–10518. Curran Associates, Inc., 2019. 6, 18
- [71] Yichen Xie, Han Lu, Junchi Yan, Xiaokang Yang, Masayoshi Tomizuka, and Wei Zhan. Active finetuning: Exploiting annotation budget in the pretraining-finetuning paradigm. In *Proceedings of the IEEE/CVF Conference on Computer Vision and Pattern Recognition*, pages 23715–23724, 2023. 1
- [72] Yazhou Yang and Marco Loog. Active learning using uncertainty information. In *2016 23rd International Conference on Pattern Recognition*. IEEE, 2016. 1
- [73] Tao Yu, Zhihe Lu, Xin Jin, Zhibo Chen, and Xinchao Wang. Task residual for tuning vision-language models. In *Proceedings of the IEEE/CVF Conference on Computer Vision and Pattern Recognition*, pages 10899–10909, 2023. 1
- [74] Xiaohua Zhai, Basil Mustafa, Alexander Kolesnikov, and Lucas Beyer. Sigmoid loss for language image pre-training. In *Proceedings of the IEEE/CVF International Conference on Computer Vision*, pages 11975–11986, 2023. 1, 2, 3, 6, 7, 8
- [75] Jingyi Zhang, Jiaying Huang, Sheng Jin, and Shijian Lu. Vision-language models for vision tasks: A survey. *IEEE Transactions on Pattern Analysis and Machine Intelligence*, 2024. 1
- [76] Renrui Zhang, Rongyao Fang, Wei Zhang, Peng Gao, Kun-chang Li, Jifeng Dai, Yu Qiao, and Hongsheng Li. Tip-adapter: Training-free clip-adapter for better vision-language modeling. In *European Conference on Computer Vision*, pages 1–19. Springer, 2022. 1

- [77] Renrui Zhang, Xiangfei Hu, Bohao Li, Siyuan Huang, Hanqiu Deng, Yu Qiao, Peng Gao, and Hongsheng Li. Prompt, generate, then cache: Cascade of foundation models makes strong few-shot learners. In *Proceedings of the IEEE/CVF Conference on Computer Vision and Pattern Recognition*, pages 15211–15222, 2023. 1
- [78] Kaiyang Zhou, Jinkang Yang, Chen Change Loy, and Ziwei Liu. Conditional prompt learning for vision-language models. In *Proceedings of the IEEE/CVF Conference on Computer Vision and Pattern Recognition*, pages 16816–16825, 2022. 1

Post-hoc Probabilistic Vision-Language Models

Supplementary Material

A. Notation

We will briefly summarise the notation used throughout the paper. See Table 3 for the modality-specific notation used and Table 4 for an overview of the notation of general operands and operators.

Description	Image	Text
Input	\mathbf{x}^{IMG}	\mathbf{x}^{TXT}
Encoder	$\phi(\cdot)$	$\psi(\cdot)$
Projection matrix	\mathbf{P}	\mathbf{Q}
Embedding	\mathbf{g}	\mathbf{h}
Normalised embedding	$\hat{\mathbf{g}}$	$\hat{\mathbf{h}}$
Kronecker factors	$\mathbf{A}_{\text{IMG}}, \mathbf{B}_{\text{IMG}}$	$\mathbf{A}_{\text{TXT}}, \mathbf{B}_{\text{TXT}}$
Hessian matrix	\mathbf{H}_{IMG}	\mathbf{H}_{TXT}
Jacobian matrix	\mathbf{J}_{IMG}	\mathbf{J}_{TXT}

Table 3. Summary of modality-specific notation.

Description	Notation
Number of data points	n
Number of test data points	n_{test}
Number of support set points	m
Kronecker product	\otimes
Prior precision	λ
Pseudo-data count	τ

Table 4. Summary of general notation.

B. Derivations

This section provides detailed derivations of the equations presented in the main text.

B.1. Laplace Approximation

To obtain the Laplace approximation to the VLM, we first assume independence between \mathbf{P} and \mathbf{Q} . The resulting GGN approximations of \mathbf{H}_{IMG} and \mathbf{H}_{TXT} are then given in form of their Kronecker factors \mathbf{A} and \mathbf{B} , *i.e.*,

$$\mathbf{H}_{\text{IMG}} \approx \left(\sqrt{\tau} \mathbf{A}_{\text{IMG}} + \sqrt{\lambda} \mathbf{I} \right) \otimes \left(\sqrt{\tau} \mathbf{B}_{\text{IMG}} + \sqrt{\lambda} \mathbf{I} \right), \quad (21)$$

$$\mathbf{H}_{\text{TXT}} \approx \left(\sqrt{\tau} \mathbf{A}_{\text{TXT}} + \sqrt{\lambda} \mathbf{I} \right) \otimes \left(\sqrt{\tau} \mathbf{B}_{\text{TXT}} + \sqrt{\lambda} \mathbf{I} \right), \quad (22)$$

where $\lambda \geq 0$ is the precision parameter of the prior and $\tau \geq 0$ is a pseudo-data count. The respective factors are given as:

$$\mathbf{A}_{\text{IMG}} = \frac{1}{\sqrt{n}} \sum_{i=1}^n \phi(\mathbf{x}_i^{\text{IMG}}) \phi(\mathbf{x}_i^{\text{IMG}})^\top \quad (23)$$

$$\mathbf{A}_{\text{TXT}} = \frac{1}{\sqrt{n}} \sum_{i=1}^n \phi(\mathbf{x}_i^{\text{TXT}}) \phi(\mathbf{x}_i^{\text{TXT}})^\top, \quad (24)$$

and

$$\mathbf{B}_{\text{IMG}} = \frac{1}{\sqrt{n}} \sum_{i=1}^n \mathbf{J}_{\text{IMG}}(\mathbf{x}_i^{\text{IMG}})^\top \mathbf{\Lambda}_{\text{IMG}} \mathbf{J}_{\text{IMG}}(\mathbf{x}_i^{\text{IMG}}) \quad (25)$$

$$\mathbf{B}_{\text{TXT}} = \frac{1}{\sqrt{n}} \sum_{i=1}^n \mathbf{J}_{\text{TXT}}(\mathbf{x}_i^{\text{TXT}})^\top \mathbf{\Lambda}_{\text{TXT}} \mathbf{J}_{\text{TXT}}(\mathbf{x}_i^{\text{TXT}}), \quad (26)$$

where n is the number image-text pairs in the training set.

Marginal Likelihood To learn the prior precision parameter, we follow prior work (*e.g.*, [32]) and optimize the log marginal likelihood, *i.e.*,

$$\log p(\mathcal{D}) \approx \log p(\mathcal{D} \mid \mathbf{P}_{\text{MAP}}, \mathbf{Q}_{\text{MAP}}) \quad (27)$$

$$- 1/2 \left(\left| \frac{1}{2\pi} \mathbf{H}_{\text{IMG}} \right| \times \left| \frac{1}{2\pi} \mathbf{H}_{\text{TXT}} \right| \right), \quad (28)$$

using gradient-based optimization.

Posterior Predictive Distribution For completeness, we will briefly derive the posterior predictive distribution and use an expression in form of a matrix normal distribution for conciseness. In particular, for the image encoder let $\mathbf{P} \sim \mathcal{MN}(\mathbf{P}_{\text{MAP}}, \mathbf{B}_{\text{IMG}}^{-1}, \mathbf{A}_{\text{IMG}}^{-1})$, then:

$$\mathbf{g} = \mathbf{P} \phi(\mathbf{x}^{\text{IMG}}) \quad (29)$$

with $\mathbf{P} \phi(\mathbf{x}^{\text{IMG}}) \sim$

$$\begin{aligned} & \mathcal{MN}(\mathbf{P}_{\text{MAP}} \phi(\mathbf{x}^{\text{IMG}}), \mathbf{B}_{\text{IMG}}^{-1}, \phi(\mathbf{x}^{\text{IMG}})^\top \mathbf{A}_{\text{IMG}}^{-1} \phi(\mathbf{x}^{\text{IMG}})) \\ \mathbf{g} & \sim \mathcal{N}(\mathbf{P}_{\text{MAP}} \phi(\mathbf{x}^{\text{IMG}}), (\phi(\mathbf{x}^{\text{IMG}})^\top \mathbf{A}_{\text{IMG}}^{-1} \phi(\mathbf{x}^{\text{IMG}})) \mathbf{B}_{\text{IMG}}^{-1}). \end{aligned} \quad (30)$$

Jacobians for the GGN Approximation In the following we derive the Jacobians $\mathbf{J}_{\text{IMG}}(\mathbf{x}_i^{\text{IMG}})$ and $\mathbf{J}_{\text{TXT}}(\mathbf{x}_i^{\text{TXT}})$ used in the Kronecker-factored Generalized Gauss-Newton (GGN) approximation of the Hessian matrices.

Let $\hat{\mathbf{g}}_i$ and $\hat{\mathbf{h}}_j$ denote the normalized image and text embedding, respectively. With some misuse of notation, let $\hat{\mathbf{H}}$ denote the matrix of normalized text embeddings with

$\hat{\mathbf{h}}_j$ as its columns, and $\hat{\mathbf{G}}$ the matrix of normalized image embeddings with $\hat{\mathbf{g}}_i$ as its columns. Then, for the InfoNCE likelihood, which depends on the dot product between the normalized embedding in the batch, we compute the Jacobian for the image encoder as follows:

$$J_{\text{IMG}}^{\text{InfoNCE}}(\mathbf{x}_i^{\text{IMG}})^\top = \frac{\partial \hat{\mathbf{H}}^\top \hat{\mathbf{g}}_i}{\partial \mathbf{g}_i} \quad (31)$$

$$= \hat{\mathbf{H}}^\top \frac{\partial}{\partial \mathbf{g}_i} \frac{\mathbf{g}_i}{\|\mathbf{g}_i\|} \quad (32)$$

$$= \hat{\mathbf{H}}^\top \frac{\|\mathbf{g}_i\| - \mathbf{g}_i \frac{\partial \|\mathbf{g}_i\|}{\partial \mathbf{g}_i}}{\|\mathbf{g}_i\|^2} \quad (33)$$

$$= \hat{\mathbf{H}}^\top \frac{\|\mathbf{g}_i\| - \frac{\mathbf{g}_i \mathbf{g}_i^\top}{\|\mathbf{g}_i\|}}{\|\mathbf{g}_i\|^2} \quad (34)$$

$$= \hat{\mathbf{H}}^\top \left(\frac{\mathbf{1}}{\|\mathbf{g}_i\|} - \frac{\mathbf{g}_i \mathbf{g}_i^\top}{\|\mathbf{g}_i\|^3} \right). \quad (35)$$

Analogously we obtain the Jacobian for the text encoder given as:

$$J_{\text{TXT}}^{\text{InfoNCE}}(\mathbf{x}_i^{\text{TXT}})^\top = \hat{\mathbf{G}}^\top \left(\frac{\mathbf{1}}{\|\mathbf{h}_i\|} - \frac{\mathbf{h}_i \mathbf{h}_i^\top}{\|\mathbf{h}_i\|^3} \right). \quad (36)$$

For SigLIP, we obtain the following Jacobians:

$$J_{\text{IMG}}^{\text{SigLIP}}(\mathbf{x}_i^{\text{IMG}})^\top = \frac{\partial \hat{\mathbf{g}}_i}{\partial \mathbf{g}_i} = \left(\frac{\mathbf{1}}{\|\mathbf{g}_i\|} - \frac{\mathbf{g}_i \mathbf{g}_i^\top}{\|\mathbf{g}_i\|^3} \right), \quad (37)$$

and

$$J_{\text{TXT}}^{\text{SigLIP}}(\mathbf{x}_i^{\text{TXT}})^\top = \frac{\partial \hat{\mathbf{h}}_i}{\partial \mathbf{h}_i} = \left(\frac{\mathbf{1}}{\|\mathbf{h}_i\|} - \frac{\mathbf{h}_i \mathbf{h}_i^\top}{\|\mathbf{h}_i\|^3} \right). \quad (38)$$

Likelihood Hessian for InfoNCE The zero-shot classifier induced by CLIP computes unnormalised logits for each class c , represented by $\hat{\mathbf{g}}_i^\top \hat{\mathbf{h}}_c =: f_c$. By applying the softmax function, we calculate the probabilities for each class c as $\pi_c = \frac{\exp(f_c)}{\sum_{c'} \exp(f_{c'})}$. The likelihood Hessian of the cross-entropy loss for this classifier is represented by

$$\Lambda_{\text{IMG}}^{\text{InfoNCE}} = \text{diag}(\boldsymbol{\pi}) - \boldsymbol{\pi} \boldsymbol{\pi}^\top. \quad (39)$$

Similarly, the likelihood Hessian for the text encoder follows analogous principles in the text-to-image direction. For a more detailed derivation of the likelihood Hessian, we refer to [54, Ch. 3.5]. Rearranging terms in the analytical expression for $J_{\text{IMG}}^\top \Lambda_{\text{IMG}}^{\text{InfoNCE}} J_{\text{IMG}}$ facilitates space-efficient computation of the GGN approximation.

Likelihood Hessian for SigLIP The SigLIP loss is defined

as follows

$$\mathcal{L}_{\text{SigLIP}}(\mathbf{X}^{\text{IMG}}, \mathbf{X}^{\text{TXT}}) \quad (40)$$

$$= -\frac{1}{n} \sum_{i=1}^n \sum_{j=1}^n \log \frac{1}{1 + \exp(-z_{ij}(t \hat{\mathbf{g}}_i^\top \hat{\mathbf{h}}_j + b))} \quad (41)$$

$$= \frac{1}{n} \sum_{i=1}^n \sum_{j=1}^n \underbrace{-\log \sigma(a_{ij})}_{:=\ell(\hat{\mathbf{g}}_i, \hat{\mathbf{h}}_j)}, \quad (42)$$

where $\sigma(a) = \frac{1}{1+e^{-a}}$ denotes the sigmoid function, and $a_{ij} := z_{ij}(t \hat{\mathbf{g}}_i^\top \hat{\mathbf{h}}_j + b)$, with labels $z_{ij} \in \{-1, 1\}$, a learnable temperature scaling parameter t , and a learnable bias b .

In order to derive the loss Hessian Λ^{SigLIP} , we first derive the component-wise loss gradient of ℓ :

$$\frac{\partial}{\partial \hat{\mathbf{g}}_k} \ell(\hat{\mathbf{g}}_i, \hat{\mathbf{h}}_j) \stackrel{i \neq k}{=} 0 \quad (43)$$

$$\frac{\partial}{\partial \hat{\mathbf{g}}_k} \ell(\hat{\mathbf{g}}_i, \hat{\mathbf{h}}_j) \stackrel{i=k}{=} \frac{\partial}{\partial \hat{\mathbf{g}}_k} -\log \sigma(a_{ij}) \quad (44)$$

$$= -\frac{1}{\sigma(a_{ij})} \frac{\partial \sigma(a_{ij})}{\partial a_{ij}} \frac{\partial a_{ij}}{\partial \hat{\mathbf{g}}_k} \quad (45)$$

$$= (\sigma(a_{ij}) - 1) z_{ij} t \hat{\mathbf{h}}_j, \quad (46)$$

which we utilise to derive the component-wise loss Hessian

$$\frac{\partial^2}{\partial \hat{\mathbf{g}}_k \partial \hat{\mathbf{g}}_k^\top} \ell(\hat{\mathbf{g}}_i, \hat{\mathbf{h}}_j) \stackrel{i \neq k}{=} 0 \quad (47)$$

$$\frac{\partial^2}{\partial \hat{\mathbf{g}}_k \partial \hat{\mathbf{g}}_k^\top} \ell(\hat{\mathbf{g}}_i, \hat{\mathbf{h}}_j) \quad (48)$$

$$\stackrel{i=k}{=} \frac{\partial}{\partial \hat{\mathbf{g}}_k^\top} \left(\sigma(a_{ij}) z_{ij} t \hat{\mathbf{h}}_j - z_{ij} t \hat{\mathbf{h}}_j \right) \quad (49)$$

$$= z_{ij} t \hat{\mathbf{h}}_k \frac{\partial \sigma(a_{ij})}{\partial a_{ij}} \frac{\partial a_{ij}}{\partial \hat{\mathbf{g}}_k^\top} \quad (50)$$

$$= t^2 \sigma(a_{ij}) (1 - \sigma(a_{ij})) \hat{\mathbf{h}}_j \hat{\mathbf{h}}_j^\top. \quad (51)$$

Finally, the likelihood Hessian for the SigLIP loss $\mathcal{L}_{\text{SigLIP}}$ can be expressed as

$$\Lambda_{\text{IMG}}^{\text{SigLIP}} = \frac{\partial^2}{\partial \hat{\mathbf{g}}_i \partial \hat{\mathbf{g}}_i^\top} \mathcal{L}(\hat{\mathbf{g}}_{1:n}, \hat{\mathbf{h}}_{1:n}) \quad (52)$$

$$= \frac{1}{n} \sum_{j=1}^n \sum_{i=1}^n \frac{\partial^2}{\partial \hat{\mathbf{g}}_i \partial \hat{\mathbf{g}}_i^\top} \ell(\hat{\mathbf{g}}_i, \hat{\mathbf{h}}_j) \quad (53)$$

$$= \frac{t^2}{n} \sum_{j=1}^n \sigma(a_{ij}) (1 - \sigma(a_{ij})) \hat{\mathbf{h}}_j \hat{\mathbf{h}}_j^\top \quad (54)$$

for the image encoder and as

$$\Lambda_{\text{TXT}}^{\text{SigLIP}} = \frac{t^2}{n} \sum_{i=1}^n \sigma(a_{ij}) (1 - \sigma(a_{ij})) \hat{\mathbf{g}}_i \hat{\mathbf{g}}_i^\top \quad (55)$$

for the text encoder.

B.2. Distribution over Cosine Similarities

For the derivation of the distribution over cosine similarities, first recall the definition of the cosine similarity between two vectors, \mathbf{g} and \mathbf{h} , which is given as $S_{\cos}(\mathbf{g}, \mathbf{h}) = \frac{\mathbf{g}^\top \mathbf{h}}{\|\mathbf{g}\| \|\mathbf{h}\|}$. Now, with some abuse of notation, let \mathbf{g} and \mathbf{h} denote random vectors for the image and text embeddings, respectively. Further, let us assume that their distribution follows a Gaussian distribution with mean $\boldsymbol{\mu}_{\mathbf{g}} = (\mu_{\mathbf{g},1}, \dots, \mu_{\mathbf{g},d})$ and $\boldsymbol{\mu}_{\mathbf{h}} = (\mu_{\mathbf{h},1}, \dots, \mu_{\mathbf{h},d})$ and diagonal covariance structure, *i.e.*, $\boldsymbol{\Sigma}_{\mathbf{g}} = \text{diag}(\sigma_{\mathbf{g},1}^2, \dots, \sigma_{\mathbf{g},d}^2)$ and $\boldsymbol{\Sigma}_{\mathbf{h}} = \text{diag}(\sigma_{\mathbf{h},1}^2, \dots, \sigma_{\mathbf{h},d}^2)$.

Then the expected value of the cosine similarity is:

$$\mathbb{E}[S_{\cos}(\mathbf{g}, \mathbf{h})] = \frac{\mathbb{E}[\mathbf{g}^\top \mathbf{h}]}{\mathbb{E}[\|\mathbf{g}\|] \mathbb{E}[\|\mathbf{h}\|]} \quad (56)$$

$$= \frac{\sum_i^d \mu_{\mathbf{g},i} \mu_{\mathbf{h},i}}{\mathbb{E}[\|\mathbf{g}\|] \mathbb{E}[\|\mathbf{h}\|]}. \quad (57)$$

Note that computing $\mathbb{E}[\|\mathbf{x}\|]$ is intractable, and we therefore bound the expected value by application of the triangle inequality, *i.e.*,

$$\mathbb{E}[\|\mathbf{x}\|] \leq \sqrt{\sum_i \mu_{\mathbf{x},i}^2 + \sigma_{\mathbf{x},i}^2}, \quad (58)$$

where we use the fact that $\mathbb{E}[x^2] = \mu_x^2 + \sigma_x^2$. Consequently, we obtain an approximation to the expected value of the cosine similarity given by:

$$\mathbb{E}[S_{\cos}(\mathbf{g}, \mathbf{h})] \approx \frac{\sum_i \mu_{\mathbf{g},i} \mu_{\mathbf{h},i}}{\sqrt{\sum_i \mu_{\mathbf{g},i}^2 + \sigma_{\mathbf{g},i}^2} \sqrt{\sum_i \mu_{\mathbf{h},i}^2 + \sigma_{\mathbf{h},i}^2}}. \quad (59)$$

Next, we will derive the second moment (variance) of the cosine similarity of two random vectors. First note that the variance can be written as the difference of two expectations, *i.e.*,

$$\text{Var}[S_{\cos}(\mathbf{g}, \mathbf{h})] = \mathbb{E}[S_{\cos}(\mathbf{g}, \mathbf{h})^2] - \mathbb{E}[S_{\cos}(\mathbf{g}, \mathbf{h})]^2, \quad (60)$$

where the second expectation corresponds to:

$$\mathbb{E}[S_{\cos}(\mathbf{g}, \mathbf{h})^2] \approx \frac{(\sum_i \mu_{\mathbf{g},i} \mu_{\mathbf{h},i})^2}{\sum_i \mu_{\mathbf{g},i}^2 + \sigma_{\mathbf{g},i}^2 \sum_i \mu_{\mathbf{h},i}^2 + \sigma_{\mathbf{h},i}^2}. \quad (61)$$

Next we can obtain $\mathbb{E}[S_{\cos}(\mathbf{g}, \mathbf{h})^2]$ for which we will use the fact that $\mathbb{E}[x^2] = \mu_x^2 + \sigma_x^2$ again, *i.e.*,

$$\mathbb{E}[S_{\cos}(\mathbf{g}, \mathbf{h})^2] = \frac{\mathbb{E}[(\mathbf{g}^\top \mathbf{h})^2]}{\sum_i \mu_{\mathbf{g},i}^2 + \sigma_{\mathbf{g},i}^2 \sum_i \mu_{\mathbf{h},i}^2 + \sigma_{\mathbf{h},i}^2} \quad (62)$$

where

$$\mathbb{E}[(\mathbf{g}^\top \mathbf{h})^2] = \sum_i \sum_j \mu_{\mathbf{g},i} \mu_{\mathbf{h},i} \mu_{\mathbf{g},j} \mu_{\mathbf{h},j} \quad (63)$$

$$+ \sum_i \sigma_{\mathbf{g},i}^2 \mu_{\mathbf{h},i}^2 + \mu_{\mathbf{g},i}^2 \sigma_{\mathbf{h},i}^2 + \sigma_{\mathbf{g},i}^2 \sigma_{\mathbf{h},i}^2. \quad (64)$$

Henceforth, we obtain for the variance:

$$\text{Var}[S_{\cos}(\mathbf{g}, \mathbf{h})] = \frac{\sum_i \sigma_{\mathbf{g},i}^2 (\sigma_{\mathbf{h},i}^2 + \mu_{\mathbf{h},i}^2) + \sigma_{\mathbf{h},i}^2 \mu_{\mathbf{g},i}^2}{\sum_i \mu_{\mathbf{g},i}^2 + \sigma_{\mathbf{g},i}^2 \sum_i \mu_{\mathbf{h},i}^2 + \sigma_{\mathbf{h},i}^2}. \quad (65)$$

C. Technical Details

This section provides further details on the support set selection strategies used in this work.

C.1. Targeted Selection

To target the active learning process towards relevant areas in the data space, we perform a k -nearest neighbours (k -NN) search around the test data. The main idea behind our adaptive targeted region selection is illustrated in Fig. 6.

Specifically, we greedily acquire an intermediate candidate set $\mathcal{T}^* \subseteq \mathcal{D}_{\text{train}}$ using k -NN selection based on the test set $\mathcal{D}_{\text{test}}$. For this, we need to compute a metric comparing the random feature projections. We assessed two different ways, first by computing the 2-Wasserstein distance between the distributions of the embeddings and the second computing the expected cosine similarity based on App. B.2. Recall that for multivariate Gaussian distributions, the 2-Wasserstein distance exists in closed-form and is given as $W_2^2(\mathcal{N}(\boldsymbol{\mu}_1, \boldsymbol{\Sigma}_1), \mathcal{N}(\boldsymbol{\mu}_2, \boldsymbol{\Sigma}_2)) =$

$$\|\boldsymbol{\mu}_1 - \boldsymbol{\mu}_2\|_2^2 + \text{tr} \left(\boldsymbol{\Sigma}_1 + \boldsymbol{\Sigma}_2 - 2(\boldsymbol{\Sigma}_1^{1/2} \boldsymbol{\Sigma}_2 \boldsymbol{\Sigma}_1^{1/2})^{1/2} \right), \quad (66)$$

where $\|\cdot\|_2$ denotes the Euclidean norm, $\text{tr}(\cdot)$ is the trace operator, and $\boldsymbol{\Sigma}^{1/2}$ is the matrix square root of $\boldsymbol{\Sigma}$. As computing the Wasserstein distance exactly is computationally and memory intensive due to the matrix square root, we approximate it by assuming both distributions to be isotropic. Hence, simplifying to $W_2^2(\mathcal{N}(\boldsymbol{\mu}_1, \boldsymbol{\Sigma}_1), \mathcal{N}(\boldsymbol{\mu}_2, \boldsymbol{\Sigma}_2)) =$

$$\sum_{i=1}^d (\mu_{1,i} - \mu_{2,i})^2 + \sigma_{1,i}^2 + \sigma_{2,i}^2 - 2\sigma_{1,i}\sigma_{2,i}, \quad (67)$$

where $\boldsymbol{\Sigma}_1 = \text{diag}(\sigma_{1,1}^2, \dots, \sigma_{1,d}^2)$ and $\boldsymbol{\Sigma}_2$ is given respectively.

Based on a selected metric, we select the training samples closest to the test set in the joint embedding space, resulting in:

$$\mathcal{T} = \bigcup_{\mathbf{g}^* \in \mathcal{T}^*} N_k(\mathbf{g}^*, \mathcal{D}_{\text{train}}), \quad (68)$$

with $N_k(\mathbf{g}^*, \mathcal{D}_{\text{train}})$ denoting the set of k -nearest neighbours of \mathbf{g}^* in the training set $\mathcal{D}_{\text{train}}$. To ensure that we select k distinct data points for each test sample, we perform an iterative search in which we discard already selected training samples and iteratively increase the search radius until k distinct samples are found for each test datum. This process is illustrated in Fig. 7.

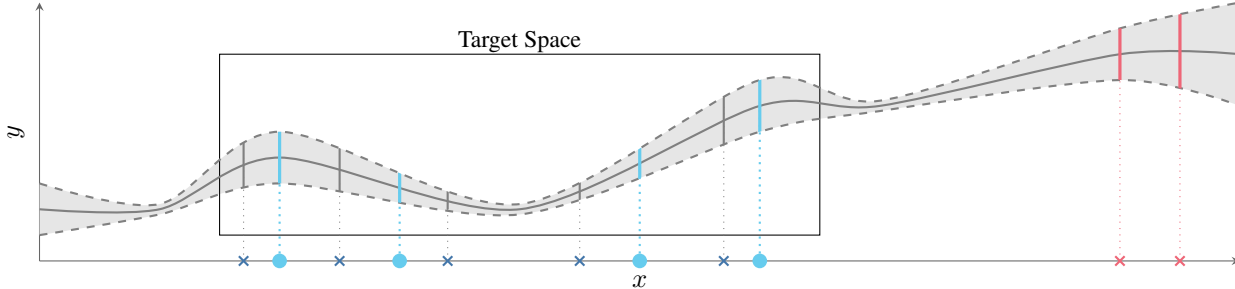


Figure 6. Illustration of targeted support set selection. We aim to select an **informative** support set that reduces the uncertainty over the predictions on the query set \bullet . Only focusing on the epistemic uncertainties would not lead to a good selection as we would select **uninformative** support set candidates \times with high epistemic uncertainty. Hence, we target the selection process.

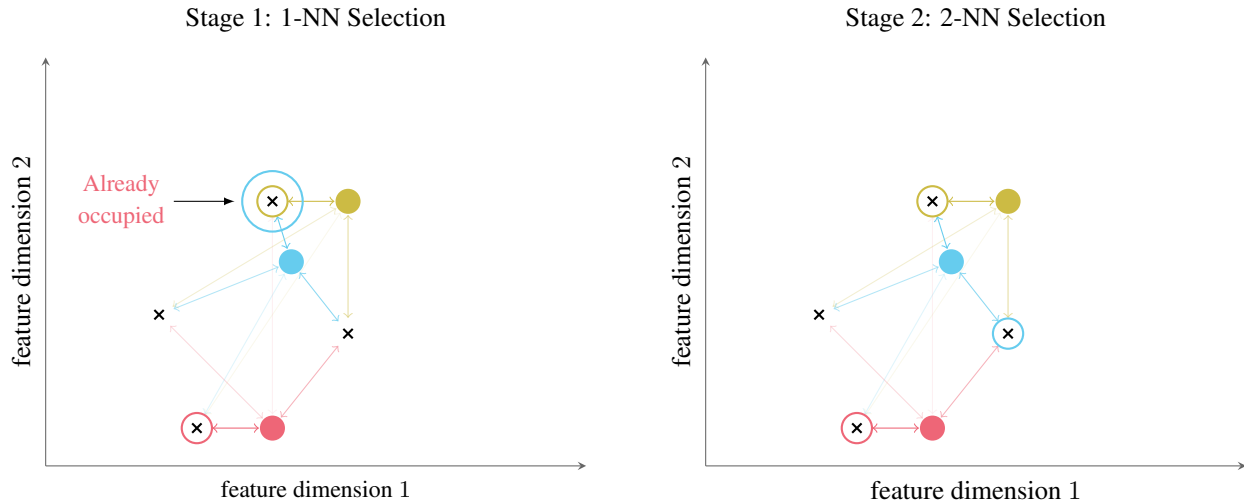


Figure 7. Illustration of the nearest neighbour based support set selection for adaptive targeted selection. The circles \bullet show test data points with uncertainty scores depicted through their colours: **high**, **medium**, **low**. For each test datum we find the $k = 1$ nearest neighbour from the support set candidates \times . If the $k = 1$ nearest neighbour is already selected, we increase k for those with occupied neighbours and choose the second nearest neighbour, *i.e.*, $k = 2$. This recursion continues until every test datum has a selected support set candidate. The selected candidates are shown by coloured circles. Note that in case of the **blue** test datum, the closest support set candidate has already been chosen by the **yellow** and hence the second closes candidate is selected in the second stage.

C.2. Acquisition Functions

In the following section, we provide a detailed explanation of the acquisition function used. Here, $\mathcal{X}_{\text{test}}$ represents the unlabelled test dataset, $\mathcal{D}_{\text{test}}$.

Naive Random For the *naive random* acquisition function, we randomly sample m data points from the train set $\mathcal{D}_{\text{train}}$ to form the support set \mathcal{S}_{ID} .

Targeted Random For the *targeted random* acquisition function, we randomly sample m data points from the unlabelled test set $\mathcal{X}_{\text{test}}$ to form an intermediate support set \mathcal{T}^* . According to App. C.1, we then select the nearest neighbours to \mathcal{T}^* from the training set $\mathcal{D}_{\text{train}}$ based on the cosine similarity of the normalized image embeddings to form the support set $\mathcal{T}_{\text{t-ID}}$.

Targeted Maximum Entropy For the *entropy* acquisition function, we compute the predictive entropy $\mathcal{H}(y_i^* | \mathbf{x}_i^*)$ for each data point $\mathbf{x}_i^* \in \mathcal{X}_{\text{test}}$ and select the m data points with the highest entropy. We use the predictive entropy on the MAP estimate of the model parameters to estimate the predictive entropy of the model:

$$\begin{aligned} \mathcal{H}(y | \mathbf{x}, \theta_{\text{MAP}}) \\ = - \sum_{c=1}^C p(y = c | \mathbf{x}, \theta_{\text{MAP}}) \log p(y = c | \mathbf{x}, \theta_{\text{MAP}}) \end{aligned} \quad (69)$$

According to App. C.1, we then select the most similar data points from $\mathcal{X}_{\text{train}}$ to form the support set $\mathcal{T}_{\text{t-entropy}}$.

BALD We compute the BALD score [26] for each data

point in $\mathcal{X}_{\text{train}}$ and select the m data points with the highest score. The score is approximated using nested Monte Carlo sampling, as in [26].

$$\text{BALD}(\mathbf{x}) \quad (70)$$

$$= \mathbb{E}_{p(y|\mathbf{x})} [\mathcal{H}(p(\boldsymbol{\theta})) - \mathcal{H}(p(\boldsymbol{\theta} | \mathbf{x}, y))] \quad (71)$$

$$= \mathbb{E}_{p(\boldsymbol{\theta}|\mathcal{D})} [\mathcal{H}(p(y | \mathbf{x}, \boldsymbol{\theta})) - \mathcal{H}(p(y | \mathbf{x}, \mathcal{D}))] \quad (72)$$

Targeted BALD We compute the BALD score (Eq. (72))

for each data point $\mathbf{x}_i^* \in \mathcal{X}_{\text{test}}$ and select the m data points with the highest score. According to App. C.1, we then select the most similar data points from $\mathcal{X}_{\text{train}}$ to form the support set $\mathcal{T}_{t\text{-BALD}}$.

EPIG The Expected Predictive Information Gain (EPIG) score [2] calculates the expected mutual information between the model parameters and the predictive distribution resulting from the acquisition of a training data point. This method is specifically designed to target relevant information, eliminating the need for a k -nearest neighbour search typically used in other acquisition functions. The EPIG score is given by

$$\text{EPIG}(\mathbf{x})$$

$$= \mathbb{E}_{p_*(\mathbf{x}^*)p(y|\mathbf{x})} [\mathcal{H}(p(y^* | \mathbf{x}^*)) - \mathcal{H}(p(y^* | \mathbf{x}^*, \mathbf{x}, y))] \quad (73)$$

$$= \mathbb{E}_{p_*(\mathbf{x}^*)} [\text{D}_{\text{KL}}(p(y, y^* | \mathbf{x}, \mathbf{x}^*) \| p(y | \mathbf{x})p(y^* | \mathbf{x}^*))] \quad (74)$$

$$= \mathbb{E}_{p_*(\mathbf{x}^*)} \left[\sum_{y \in \mathcal{Y}} \sum_{y^* \in \mathcal{Y}} p(y, y^* | \mathbf{x}, \mathbf{x}^*) \times \log \frac{p(y, y^* | \mathbf{x}, \mathbf{x}^*)}{p(y | \mathbf{x})p(y^* | \mathbf{x}^*)} \right] \quad (75)$$

where $p_*(\mathbf{x}^*)$ denotes the target input distribution. The EPIG score is approximated using Monte Carlo sampling, as detailed in [2]. For the EPIG selection, we perform online updates to the model weights using the online Laplace as described in App. C.3.

C.3. Online Laplace Approximation

Recall, that we obtain from our post-hoc Laplace approximation the Kronecker factorized Hessian approximation $\mathbf{H}_{\text{IMG}} \approx (\sqrt{\tau} \mathbf{A}_{\text{IMG}} + \sqrt{\lambda} \mathbf{I}) \otimes (\sqrt{\tau} \mathbf{B}_{\text{IMG}} + \sqrt{\lambda} \mathbf{I})$ with

$$\mathbf{A}_{\text{IMG}} = \frac{1}{\sqrt{n}} \sum_{i=1}^n \phi(\mathbf{x}_i^{\text{IMG}}) \phi(\mathbf{x}_i^{\text{IMG}})^\top \quad \text{and} \quad (76)$$

$$\mathbf{B}_{\text{IMG}} = \frac{1}{\sqrt{n}} \sum_{i=1}^n \mathbf{J}_{\text{IMG}}(\mathbf{x}_i^{\text{IMG}})^\top \boldsymbol{\Lambda}_{\text{IMG}} \mathbf{J}_{\text{IMG}}(\mathbf{x}_i^{\text{IMG}}), \quad (77)$$

approximating a posterior distribution over the projection weights:

$$\mathbf{P} \sim \mathcal{MN}(\mathbf{P}_{\text{MAP}}, \tilde{\mathbf{B}}_{\text{IMG}}^{-1}, \tilde{\mathbf{A}}_{\text{IMG}}^{-1}) \quad (78)$$

$$\mathbf{Q} \sim \mathcal{MN}(\mathbf{Q}_{\text{MAP}}, \tilde{\mathbf{B}}_{\text{TXT}}^{-1}, \tilde{\mathbf{A}}_{\text{TXT}}^{-1}) \quad (79)$$

with $\tilde{\mathbf{A}}, \tilde{\mathbf{B}}$ denoting the Kronecker factors after applying τ and λ .

Further, utilizing App. B.2 in combination with the generalized probit approximation (as described, for instance, in [15]) we obtain an analytical form for the predictive posterior distribution $p(y | \mathbf{x}, \mathcal{D})$ of our few-shot classifier.

Our goal with EPIG is to iteratively construct a support set \mathcal{T}_t , where t denotes the current number of selected training data points. We construct \mathcal{T}_t by greedily selecting the training datum that maximizes the expected information gain on the predictive distribution in the target domain:

$$\mathbf{x}_{t+1} = \arg \max_{\mathbf{x} \in \mathcal{D}_{\text{train}}} \text{EPIG}(\mathbf{x} | \mathcal{T}_t) \quad (80)$$

$$= \arg \max_{\mathbf{x} \in \mathcal{D}_{\text{train}}} \mathbb{E}_{p_*(\mathbf{x}^*)p(y|\mathbf{x})} [\mathcal{H}(p(y^* | \mathbf{x}^*, \mathcal{T}_t)) - \mathcal{H}(p(y^* | \mathbf{x}^*, \mathcal{T}_t \cup \{(\mathbf{x}, y)\}))] \quad (81)$$

and obtain the corresponding label y_{t+1} , forming the support set $\mathcal{T}_{t+1} = \mathcal{T}_t \cup \{(\mathbf{x}_{t+1}, y_{t+1})\}$.

The integration of $\{(\mathbf{x}_{t+1}, y_{t+1})\}$ into the few-shot training set changes the posterior distribution over the image projection. To obtain the updated posterior distribution

$$\mathbf{P} | \mathcal{T}_{t+1} \sim \mathcal{MN}(\mathbf{P}_{\text{MAP}}, \tilde{\mathbf{B}}_{\text{IMG}, t+1}^{-1}, \tilde{\mathbf{A}}_{\text{IMG}, t+1}^{-1}), \quad (82)$$

we utilise the following online updates to the projection weights and the Laplace approximation:

$$\mathbf{P}_{\text{MAP}, t+1} = \mathbf{P}_{\text{MAP}, t} - \gamma \nabla_{\mathbf{P}} \mathcal{L}(\mathbf{x}_{t+1}^{\text{IMG}}, \mathbf{X}^{\text{TXT}}) \quad (83)$$

$$\mathbf{A}_{\text{IMG}, t+1} = \frac{\sqrt{n+t} \mathbf{A}_{\text{IMG}, t} + \beta \mathbf{A}_{\mathbf{x}_{t+1}}}{\sqrt{n+t+1}} \quad (84)$$

$$\mathbf{B}_{\text{IMG}, t+1} = \frac{\sqrt{n+t} \mathbf{B}_{\text{IMG}, t} + \beta \mathbf{B}_{\mathbf{x}_{t+1}}}{\sqrt{n+t+1}}. \quad (85)$$

where $\gamma \geq 0$ and $\beta \geq 0$ are hyperparameters and

$$\mathbf{A}_{\mathbf{x}_{t+1}} = \phi(\mathbf{x}_{t+1}^{\text{IMG}}) \phi(\mathbf{x}_{t+1}^{\text{IMG}})^\top \quad (86)$$

$$\mathbf{B}_{\mathbf{x}_{t+1}} = \mathbf{J}_{\text{IMG}}(\mathbf{x}_{t+1}^{\text{IMG}})^\top \boldsymbol{\Lambda}_{\text{IMG}} \mathbf{J}_{\text{IMG}}(\mathbf{x}_{t+1}^{\text{IMG}}). \quad (87)$$

D. Experimental Details

We run experiments on a compute cluster with NVIDIA P100 16GB, V100 32 GB, and A100 80GB GPUs. We used V100 or A100 GPUs for the Huge model variants and the ImageNet experiments.

D.1. Estimation of the Hessian Matrices

We estimated the Hessians separately for the CLIP image and text encoders using the pre-training dataset LAION-400M [61]. For this estimation, we randomly sampled a subset of 327.680 data points. The pre-training dataset was filtered to exclude NSFW content. For the Laplace approximation, we used the GGN approximation of the Hessian matrices as described in App. B.1 and estimated the covariance matrices A and B for the image and text encoders.

D.2. Estimation of the Hessian Parameters

To ensure that both zero-shot and active learning experiments rely on a well-calibrated posterior covariance, we estimated the pseudo-data count [56], τ , by performing a grid search over values in $\tau \in [1, 5, 10, 15, \dots, 200]$. In the active learning experiments, the step size was reduced to 2. The optimal value of τ was selected by minimizing the negative log predictive density (NLPD) on a random subset of ImageNet consisting of 100 classes and 1097 test data points in total as a proxy. App. D.2 presents two plots illustrating the NLPD as a function of the pseudo-data count for SigLIP-Base and CLIP-Base, respectively. Once this optimal τ was identified, we further optimized the prior precision, λ , using the marginal likelihood on the LAION-400M [61] dataset.

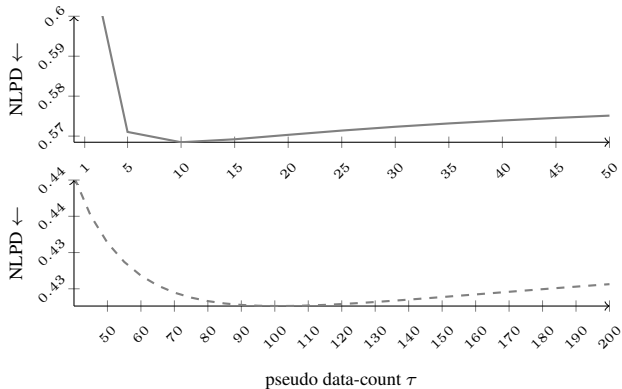


Figure 8. Grid search over the pseudo-data count parameter τ for CLIP-Base (—) and SigLIP-Base (---). The optimal NLPD for CLIP-Base is identified at $\tau = 10$, while the optimal NLPD for SigLIP-Base is identified at $\tau = 100$.

D.3. Active Learning Experiments

We conducted active learning experiments on the Office-Home data set [69], which consists of the domains: art, clipart, product, and real-world, as well as on the ImageNet dataset with the domains ImageNet-R [24] and ImageNet-Sketch [70]. For these experiments, all training sets from the respective domains were combined into a single, large training set, and the projection layer of either CLIP or SigLIP

was fine-tuned for a specific domain. Data selection was performed based on the acquisition functions described in App. C.2. Performance was evaluated at the checkpoint corresponding to the lowest NLPD on a domain-specific validation set. We also performed a grid search for the online learning parameters of the EPIG acquisition rule, selecting the EPIG learning rate γ from the range [1e-5, 1e-4, 1e-3, 1e-2] and the EPIG Hessian update scale β from [1, 10, 100, 1000], based on the NLPD on the domain-specific validation set. Detailed training procedures are provided in the following table.

D.4. Zero-shot Experiments

config	value
optimizer	AdamW
learning rate	1e-5
weight decay	5e-2
optimizer momentum	$\beta_1, \beta_2 = 0.9, 0.999$
batch size	32
epochs	100

Table 5. Active fine-tuning hyperparameters.

D.5. Approximation Quality

To assess the approximation quality of the Gaussian approximation to the distribution over cosine similarities, we generated 500 samples for the image and text feature distributions for a given input. For the resulting samples, we then computed the respective cosine similarity for each pair and performed kernel density estimation with Gaussian kernel and lengthscale of 0.3 on the similarity scores. We added increasing shifts to the distribution mean to evaluate the change in the approximation quality under varying cosine similarity values. The results are depicted in Fig. 3.

E. Additional Results

E.1. Active Learning Experiments

We report the active learning results for CLIP-Huge in Fig. 9 and for SigLIP-Base in Fig. 10. For CLIP-Huge we observe that active learning based on our post-hoc uncertainties consistently improves upon random and entropy-based selection. For SigLIP-Base, we observe significant improvements in terms of accuracy and NLPD on the ImageNet version with active learning based on our post-hoc uncertainties.

E.2. Ablation of the k -NN Distance Metric

We performed an ablation study on the k -NN distance metric for our proposed targeted selection in Sec. 3.4 while

fixing the *online LA learning rate* $\gamma = 1e-4$ and the *online LA pseudo-data count* $\beta = 10$. We evaluate performance using two distance metrics: Wasserstein and cosine similarity. Results are reported for EPIG and BALD, with Wasserstein (*solid lines*) and cosine (*dashed lines*) metrics. While Wasserstein-based k-NN selection demonstrates improved performance for datasets such as OfficeHome-Art and ImageNet-R, no clear trend is observed across the other datasets.

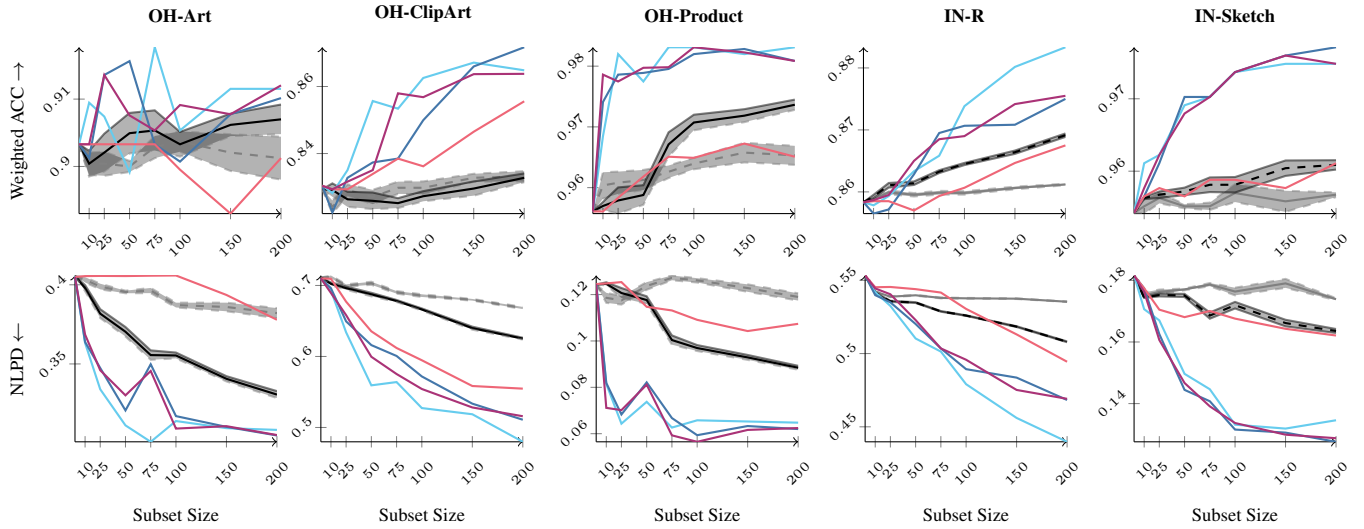


Figure 9. **Active Learning Results (CLIP Huge):** We present results for EPIG (—), BALD (—), Entropy (targeted) (—), Entropy (—), Random selection (targeted) (—), Random selection (—) on the OfficeHome dataset (OH) and ImageNet variants (IN). We observe that active learning based on our post-hoc uncertainties consistently improves upon random and entropy-based selection.

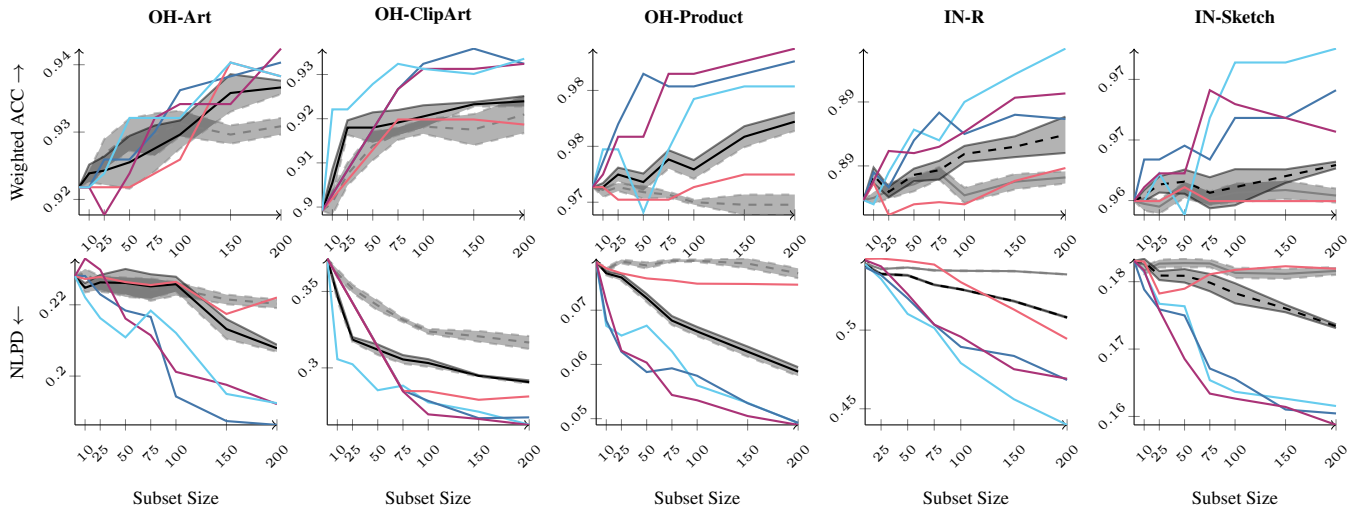


Figure 10. **Active Learning Results (SigLIP Base):** We present results for EPIG (—), BALD (—), Entropy (targeted) (—), Entropy (—), Random selection (targeted) (—), Random selection (—) on the OfficeHome dataset (OH) and ImageNet variants (IN).

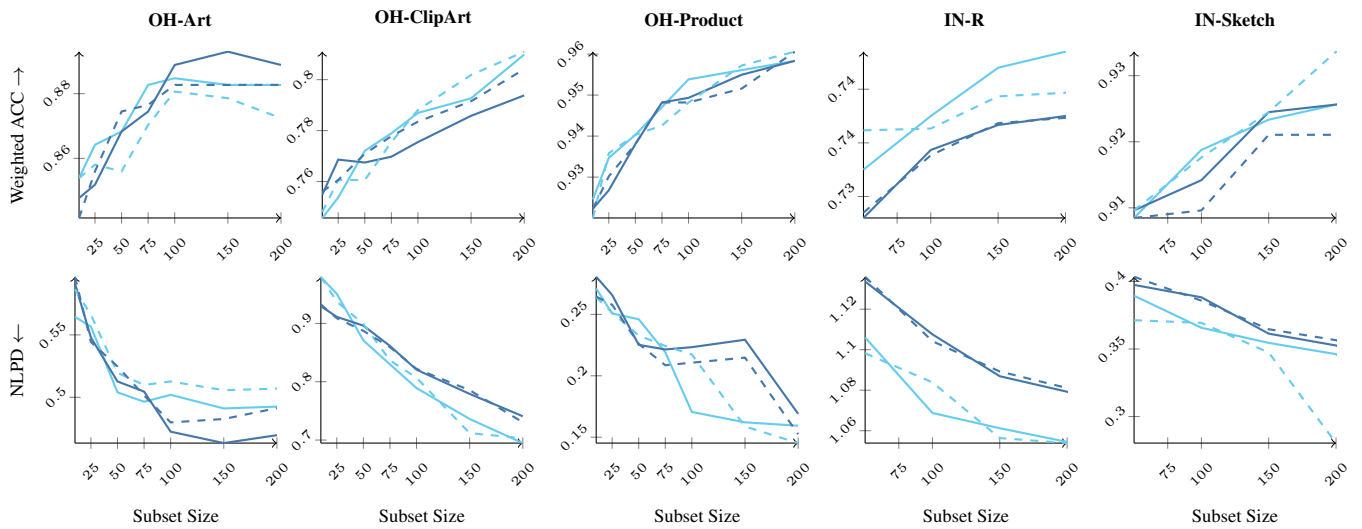


Figure 11. Ablation study on the k -NN distance metric, fixing the *online LA learning rate* $\gamma = 1e-4$ and the *online LA pseudo-data count* $\beta = 10$. Results are shown for EPIG (Wasserstein) (—), EPIG (cosine) (---), BALD (Wasserstein) (—), and BALD (cosine) (---). As shown in Fig. 11, Wasserstein-based k -NN selection demonstrates improved performance for datasets such as *OH-Art* and *IN-R*, while no clear trend is observed across the other datasets.